Synthesis and photocatalytic performance of visible-light-responsive double perovskite oxide semiconductors

Thesis by

Dayal Chandra Roy

In partial Fulfillment of the Requirements
for the Degree of Doctor of Philosophy
Doctoral Thesis 2024

Division of Fundamental and Applied Sciences
Faculty of Science and Engineering
Graduate School of Science and Engineering
Iwate Univrsity
4-3-5 Ueda, Morioka-shi, Iwate 020-8551 Japan

ABSTRACT

$A_2BB'O_6$ double perovskite oxides earned remarkable praise for obtaining good-quality solar light conversion efficiency. The large option to choose elements in A and B positions in this structure and their hybridization provides versatile scope in designing a unique photocatalyst. Numerous photocatalysts with strong photocatalytic activities have been reported. However, the charge separation mechanism related to band gap energy and the right band energy location to support photocatalytic electrochemical reactions (oxidation and reduction reactions) made them less effective as catalysts. To get an effective photocatalyst, other aspects such as surface characteristics and structural stability are also important. In this research, these important factors were considerably taken into account, and two steps have been performed to obtain excellent photocatalytic activity. In the first step, a rare-earth based double perovskite $Ba_2Tb(Bi_{1-x}Sb_x)O_6$ (x=0, 0.1, 0.5, 0.6, and 1.0) was synthesized by citrate pyrolysis technique. The choice of rare-earth elements is because their mixed valence states exhibit exceptional charge separation ability, which plays an important role in the photocatalysis process. However, the use of rare-earth elements is cost-effective, and considering this issue, in the next step, a rare-earth free $Ba_2Bi^{3+}Bi^{5+}_{1-2x}Sb^{5+}_{2x}O_6$ (x=0, 0.1, 0.2, 0.3, 0.4, and 0.5) double perovskite oxide was prepared using Solid-state technique. The effect of Sb substitution on the structural, optical, and photocatalytic properties of both samples was investigated. Rietveld refinement of X-ray diffraction pattern analysis confirmed the formation of single crystallite phases (monoclinic, rhombohedral, and cubic). The presence of Tb mixed valence states (Tb^{3+} and Tb^{4+}) in the $Ba_2Tb(Bi_{1-x}Sb_x)O_6$ samples, a typical feature of lanthanoids (Ln), was confirmed by magnetic measurement. The structural stability for both the investigated compounds was properly analyzed through tolerance factor estimation and found to be good stability under Sb substitution.

The effect of Sb substitution on B-site ordering in the $Ba_2Tb(Bi_{1-x}Sb_x)O_6$ double perovskite oxide analyzed through least square fitted X-ray diffraction data suggested a partial disordering phenomenon. Optical properties were investigated through band gap estimation by applying Kubelka-Munk function revealed band gap is a function of Sb concentrations. A band gap widening effect was seen as a result of partial Sb substitution at the Bi site, which can be attributed to the relativistic effect of the Sb 5s electronic state having a relatively higher energy than the Bi 6s electronic state. A comprehensive study based on the theoretical inquiry of density functional analysis suggested that increasing Sb values in the $Ba_2Tb(Bi_{1-x}Sb_x)O_6$ and $Ba_2Bi^{3+}Bi^{5+}_{1-2x}Sb^{5+}_{2x}O_6$ compounds caused a substantial shift of the bottom portion of the conduction band toward higher energies. The replacement of bottom part of conduction band associated with Bi^{5+}(6s) by the higher Sb^{5+}(5s) reflected to this result.

Finally, the catalytic activities were carried out from visible light facilitated reductive methylene blue (MB) degradation. The former research on Pr-based $Ba_2Pr(Bi,Sb)O_6$ double perovskite and parent $BaBiO_3$ perovskite are also considered in this research to make an analytical comparison. In case of $Ba_2Tb(Bi_{1-x}Sb_x)O_6$, the higher MB degradation performance obtained in the highly Sb substituted samples, while maximum degradation (100%) was found for 60% Sb concentration. Machine learning program introduced to this research previously suggested for 60% Sb concentration as a suitable combination satisfactorily matched with the experimental result. Comparing with other relevant compounds, $Ba_2(Pr,Tb)(Bi_{1-x}Sb_x)O_6$ exhibited even better photocatalytic conversion efficiency. The high-quality powder samples with improved surface morphology and the presence of mixed valence states of Tb and Pr ions reflected this performance. However, in $Ba_2Bi^{3+}Bi^{5+}_{1-2x}Sb^{5+}_{2x}O_6$ case, the maximum degradation (50%) observed for 20% Sb incorporated sample. The unique surface morphology and reduced particle size in the Sb-substituted samples account for their improved photocatalytic performance. Although the

$Ba_2Bi^{3+}Bi^{5+}_{1-2x}Sb^{5+}_{2x}O_6$ performance is not up to par, it is relatively good compared to Sb-free rare-earth based compounds and indicates future possibility of designing a novel photocatalyst. Sample preparation technique and charge separation mechanism are expected to be affected for $Ba_2Bi^{3+}Bi^{5+}_{1-2x}Sb^{5+}_{2x}O_6$ samples.

Furthermore, photocatalytic IPA decomposition was carried out to support the catalytic activities of the investigated compounds. However, IPA decomposition result showed a controversial relation to the MB degradation. Using band edge potential calculations on the normal hydrogen electrode potential scale (NHE), these typical behaviors were elucidated. According to NHE, it was observed that the CB edge position of heavily substituted Sb samples promoted a more efficient reduction process. As a result, samples with a higher Sb content exhibited better photocatalytic MB degradation. In contrast, the lower Sb substitute samples' band edge positions were found to be suitably promoted to more holes in the VB due to the smaller band gap that contributed to the IPA decomposition result. The findings indisputably emphasized the effectiveness of band edge position in promoting more reduction processes for excellent photocatalytic MB degradation. This research conveys a clear message about the Sb substitution-dependent possibility of tunning an oxidative to a reductive photocatalyst in the preparation of a unique photocatalyst.

Supplements

The current thesis is conducted based on the following appendices

I. **D.C. Roy**, M. Matsukawa, T. Yonai, M. Arakida, H. Taniguchi, K. Nishidate, S. Aisawa, A. Matsushita, L. Shiqi, Enhanced photocatalytic activities under visible light of double-perovskite oxide semiconductor $Ba_2Tb(Bi, Sb)O_6$ with mixed-valence, *J. Mater. Sci. Mater. Electron.* 34,281 (2023).

II. **D. C. Roy**, M. Matsukawa, M. Arakida, H. Sakou, K. Hata, K. Nishidate, S. Aisawa, H. Yamamoto, A. Matsushita, Structural, optical, and photocatalytic properties of rare-earth free double-perovskite oxides $Ba_2Bi^{3+}Bi^{5+}_{1-2x}Sb^{5+}_{2x}O_6$ *Solid State Commun.* 373, 115336 (2023).

III. A. Sato, M. Matsukawa, H. Taniguchi, S. Tsuji, K. Nishidate, S. Aisawa, A. Matsushita, K. Zhang, Structural, physical and photocatalytic properties of mixed-valence double-perovskite $Ba_2Pr(Bi, Sb)O_6$ semiconductor synthesized by citrate pyrolysis technique, *Solid State Sci.* 107,10635-1-7 (2020).

IV. T. Senzaki, M. Matsukawa, T. Yonai, H. Taniguchi, A. Matsushita, T. Sasaki, M. Hagiwara, Functional materials synthesis and physical properties, in: M. Bar-toli, M. Giorcelli (Eds.), Recent Perspectives in Pyrolysis Research, IntechOpen, Rijeka, 2021, Ch. 9.

TABLE OF CONTENTS

LIST OF FIGURES

LIST OF TABLES

TABLE **PAGE**

Abbreviations and Symbols

XRD	X-ray Diffraction
SEM	Scanning Electron Microscope
MB	Methylene Blue
LMB	Leuco Methylene Blue
IPA	Isopropanol Alcohol
KM	Kubelka-Munk
E_g	Band gap
E_g^i	Indirect Band gap
E_g^d	Direct Band gap
VB	Valence Band
CB	Conduction Band
E_{CB}	Conduction band potential
E_{VB}	Valence band potential
NHE	Normal Hydrogen Electrode
Ln	Lanthanoids
EPD	Electrophoretic Deposition
UV	Ultraviolet
IR	Infrared
μ_{eff}	Effective magnetic moment
Equ.	Equation

Chapter 1

Introduction

1 . 1 Background

Discovery of TiO_2 photocatalyst by Fujishima and Honda (in 1972) is a great relief for current and future environmental concerns regarding water contamination and the rapid depletion of natural resources [1]. Following the commercial TiO_2 photocatalyst, numerous alternative photocatalysts have been developed [2-4], owing to the higher band gap of TiO_2, which restricts its consumption to a negligible fraction (3%) of the entire solar spectrum. Besides, researchers continue to investigate this issue in an effort to develop a more effective solution.

In general, a photocatalyst is a material has the ability to convert light energy into electrochemical energy by supplying charges. The process of photocatalysis involves the emission of a photon with an energy equivalent to or greater than the band gap of the semiconductor, which induces electrons in the conduction band and holes in the valence band. These electrons and holes take part in a variety of chemical reactions with the adsorbed spices, water, oxygen, and other organic and inorganic species in the reactor. However, due to a number of factors associated with the semiconductor, photo-excited electrons and holes may recombine, releasing heat into the medium during the photocatalytic process. The electrons and holes that only migrate to the semiconductor surface without recombination undergoes catalytic reduction/oxidation reactions. An illustration of a basic photocatalysis process is shown in Figure 1.1.

However, the photocatalytic mechanism encompasses a multitude of additional factors, rendering this a truly formidable undertaking [5, 6]. As of now, the majority of published

research pertains to the structural stability [7], surface properties [8-10], and band gap mechanism [11, 12] of photocatalysts. These key factors are prerequisites for preparation of an effective photocatalyst. Here, the concept “band gap mechanism” corresponds to the photoexcited charge separation process relating to the band edge potentials associated with the photocatalytic oxidations and reduction reactions. It has been reported that for a photocatalyst to effectively carry out a photocatalytic reaction, its band edge potential must be in the minimum suitable position. Although, there are tremendous research reported on this field, photocatalyst only those band edge potentials are suitably located on that potential can be considered as an actual one. Accordingly, Suzuki demonstrated that photocatalytic reduction performance can be improved by adjusting the CB edge position to a semiconductor with a higher reduction potential [13].

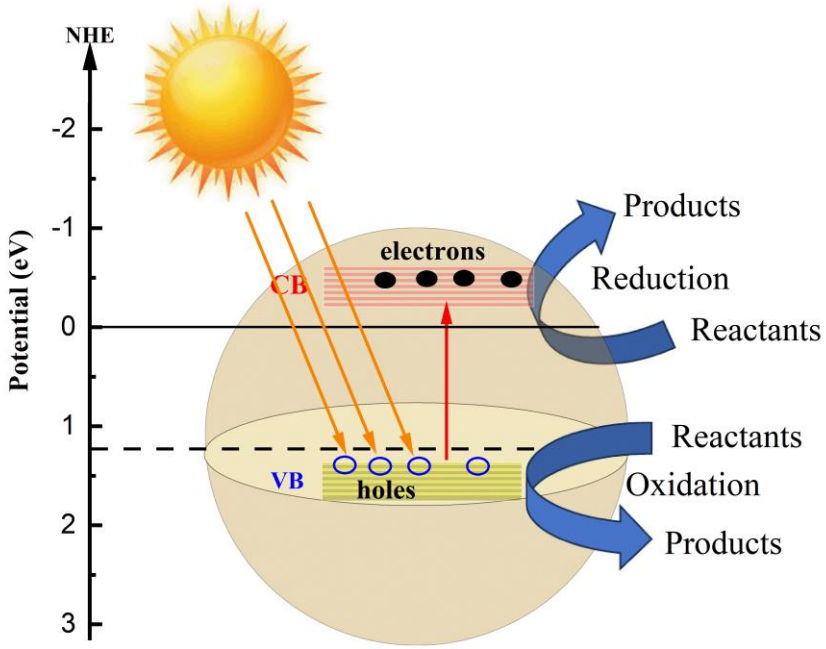

Figure 1.1: Photocatalysis process in a simplified illustration

In the recent research history, pseudo-cubic perovskite with the structure ABO_3 found in the top of the leading photocatalytic research [14-16]. The suitability of this structure in selecting larger and smaller cations and their combination in A and B site occupancy makes the compound interesting in designing a novel functional material. Another important feature of ABO_3 structure is it can be extended in a twice form like $AA^{/}BB^{/}O_6$ known as double perovskite oxides [17, 18]. The versatile options and flexibility on selecting cations at $AA^{/}$ and $BB^{/}$ site in this frame offers wider scope to extract some unconventional physical properties. There are numerous researches with diverse properties especially photocatalytic and optoelectronic properties has been established depending on the selective cations [19]. However, the utmost properties are drawn from the $A_2BB^{/}O_6$ double perovskite oxide. It is noted that $BB^{/}$ site cations and their size plays an important role in the physiochemical properties of double perovskite oxide structure. The order and disorder type structure are determined from the B and $B^{/}$ sites cations size and oxidation state difference which influence to its properties. Recently, $Ba_2BB^{/}O_6$ double perovskite where rare-earth element in B-site and Bi in $B^{/}$-site i.e., Ba_2LnBiO_6 (Ln=rare-earth elements) has been investigated and obtained good photocatalytic activities [20]. However, further research is required to explain the reason for high photocatalytic performances accurately. Recent research on Ba_2PrBiO_6 semiconductor found improvement in photocatalytic performance under the presence of mixed valence state of Pr (Pr^{3+} and Pr^{4+}) [20, 21]. The mechanism of charge separation and their effective contribution in the catalytic process are displayed in Figure 1.2.

The confirmation of Pr mixed valence state was made from the magnetic measurement of susceptibility data where the average Pr ion are found in the intermediate of Pr^{3+} and Pr^{4+} state [22, 23, 24]. Nevertheless, the mixed valence state has a great influence on photocatalytic properties, others intriguing factors and their mechanism in improvising the catalytic activities should need to be considered. In addition, to date there are no much

research reported on Ba_2LnBiO_6 semiconductor photocatalyst offers outstanding opportunity to work on this material. Moreover, the band gap magnitude is also found to be approximately in the visible range of solar spectrum. Therefore, it is expected that Ba_2LnBiO_6 can exhibits visible light driven unique photocatalytic properties.

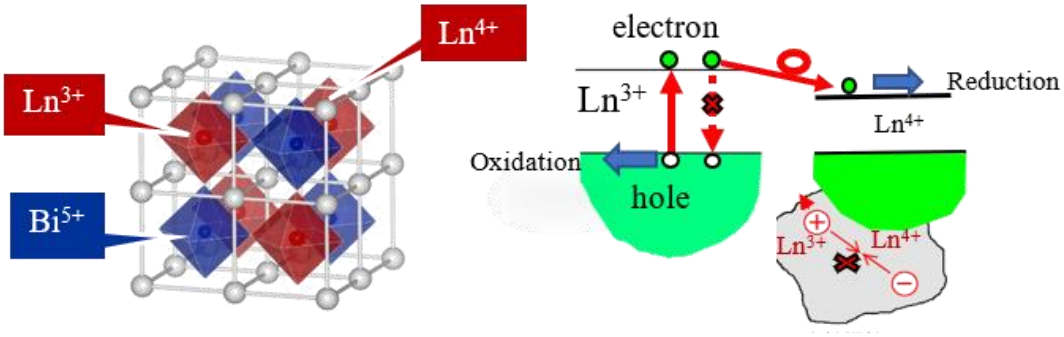

Figure 1.2: Ba_2LnBiO_6 double perovskite oxide with mixed valence states and their charge separation mechanism.

1.2 Research Motivations and objectives

The aim of this thesis is to develop visible light driven enhance photocatalytic performance of double perovskite oxide semiconductors. The exceptional charge separation ability of rare-earth elements, as explained above, made them superior for enhanced catalytic activities. Hence, rare-earth-based Ba_2LnBiO_6 double perovskite oxide photocatalyst is expected to be a great option for synthesis. In contrast, the expensiveness of rare-earth elements, it is utmost important to make an effort to prepare a rare-earth free semiconductor and compare their photocatalytic efficiency. Hence, an isostructural rare-earth free double perovskite oxide $Ba_2Bi^{3+}Bi^{5+}O_6$ can be a good option to prepare and

compare its performance with the rare-earth based Ba_2LnBiO_6 semiconductor. As discussed, crystal structural stability, surface modification, and band gap functions are the significant factors contributing to the photocatalysis reaction process considered in this research. It is expected that these factors can remarkably affect the catalyst's performance towards better efficiency. Furthermore, several efforts have been devoted to understanding the basic principle of photocatalysis.

A. Rare-earth-based double perovskite oxide

As introduced, Ba_2PrBiO_6 exhibits higher photocatalytic efficiency with the existence of Pr ion mixed valence state effectively separated the charge carriers. In connection with Pr ion, Tb ion from the rare-earth series can be considered as for the next potential candidate in the preparation of good photocatalyst.

B. Rare-earth free double perovskite oxide

Photocatalyst cost is an important factor in utilizing its properties on a large scale. In this regard, $Ba_2Bi^{3+}Bi^{5+}O_6$ a rare-earth free double perovskite semiconductor having a similar structure of Ba_2LnBiO_6, would be a great option to emphasize their photocatalytic properties.

C. Tuning band edge potential

Band edge potential in the photocatalyst plays a key role in accelerating the photo-electrochemical reaction as discussed. It is a desirable fact to position CB and VB in order to make a photocatalytic oxidation reduction reaction. In this research, the suitable position of the CB and VB edge potential and their separation at an optimum level where the visible light-induced photoexcited electrons can easily migrate to the CB as well as the surface of the catalyst before recombination have been considered. By partially incorporating Sb because of its higher energy orbital in Bi, it is expected that it will be

possible to achieve the goal. The improvisation of CB potential upon Sb substitution towards higher reduction can be reflected in better catalytic performance. An expected or proposed electronic band edge structure mechanism is illustrated in Figure 1.3. In addition, Bi and Sb exist in the same group of periodic table, having similar electronic structures, while the Sb 5s orbital is relatively higher than the Bi 5s orbital due to the relativistic effect, which can be a good option for tuning the semiconductor band gap.

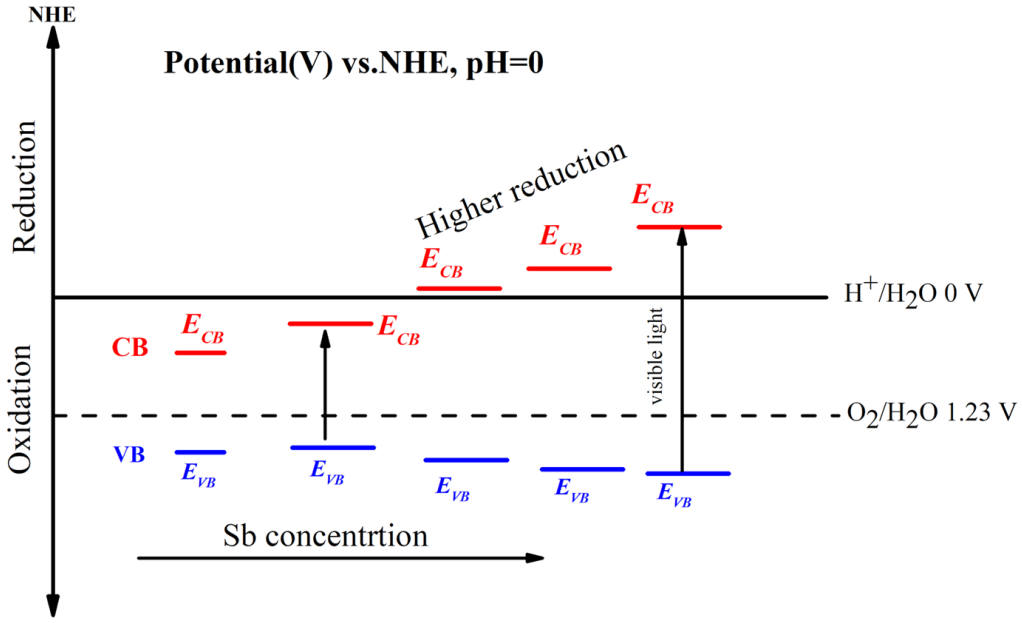

Figure 1.3: Schematic illustration of Band edge tuning higher photocatalytic reduction reaction of a semiconductor catalyst

1.3 Research objectives

- To prepare $Ba_2TbBi_{(1-x)}Sb_xO_6$ and $Ba_2Bi^{3+}Bi^{5+}_{1-2x}Sb^{5+}_{2x}O_6$double perovskite oxide following Citrate Pyrolysis and solid-state synthesis technique
- To demonstrate the Sb substitution dependent crystal structures, magnetic, optical and photocatalytic properties $Ba_2TbBi_{(1-x)}Sb_xO_6$ and $Ba_2Bi^{3+}Bi^{5+}_{1-2x}Sb^{5+}_{2x}O_6$ double perovskite oxide semiconductors
- To explore Tolerance factor dependent phase stability diagram
- To harvest maximum solar energy by optimizing band gap and promoting more charge separations in the semiconductors
- To control band edge position towards making suitable oxidative to reductive photocatalyst.

Chapter 2

Experimental Work

2.1 Sample Preparation

A. preparation of $Ba_2TbBi_{(1-x)}Sb_xO_6$

Polycrystalline $Ba_2Tb(Bi_{1-x}Sb_x)O_6$ high quality powder samples with various composition of Sb (x=0.0, 0.1, 0.2, 0.5, 0.6, and 1.0) was prepared using citrate pyrolysis synthesis method [22, 25]. A schematic flow chart diagram of citrate pyrolysis route followed to prepared $Ba_2Tb(Bi_{1-x}Sb_x)O_6$ double perovskite oxide are represented in Figure 2.1.

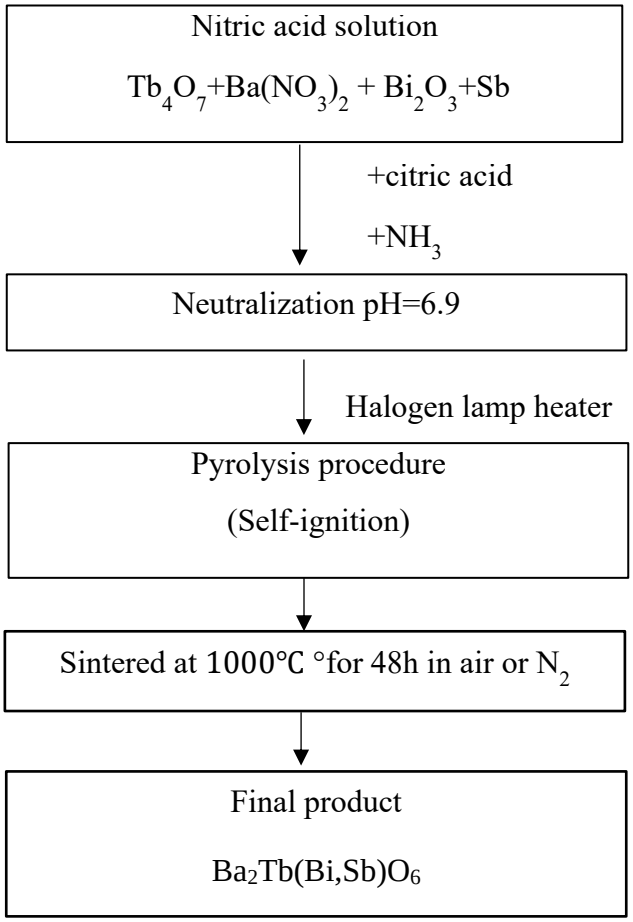

Figure 2.1: Citrate pyrolysis synthesis flow chart diagram

Initially, the stoichiometric proportion of high purity powder precursor materials $Ba(NO_3)_2$, Tb_4O_7, Bi_2O_3, and Sb were weighted and placed in beaker containing nitric acid. The beaker was then kept at temperature 70-80 ^{0}C under vigorous magnetic stirring using a hot plate magnetic stirrer until receive complete mixture solution. After that citric acid as a chelating agent was added to get a stable solution under acidic reaction. Subsequently, aqueous ammonia for the neutralization of the solution were added carefully. The final yellow-brown solution was then slowly heated using a halogen lamp stirrer. As the water evaporates the solution becomes more viscus and started self-ignition process that yielded porous products. It is noted that, in the present research, the amount of metal cations ($Ba_2Tb(Bi,Sb)O_6$), citric acid, and nitric acid were used following the molar ratio $Ba_2Tb(Bi,Sb)O_6$:$C_6H_8O_7$:HNO_3 = 1:6:10. In the next step, the obtained porous product were grounded and prepared for heat treatment. Finally, the double-perovskite phase was synthesized by grinding the precursors into fine powders and then annealing them at 900-1100 ^{0}C in air (or nitrogen gas) for 48-96 hours.

B. Preparation of $Ba_2Bi^{3+}Bi^{5+}_{1-2x}Sb^{5+}_{2x}O_6$

Solid-state synthesis [26] method was followed to prepare $Ba_2Bi^{3+}Bi^{5+}_{1-2x}Sb^{5+}_{2x}O_6$(x=0, 0.1, 0.2, 0.3,0.4, and 0.5) double perovskite oxide semiconductor. A systematic sample preparation flow chart process is presented in Figure 2.2. In the early stage, the appropriate stoichiometric proportion of 8g of high-purity $BaCO_3$ (100%), Bi_2O_3 (99%), and Sb (100%) raw chemicals were collected and placed in an agate mortar for hand mixing for few minutes. The precursor sample was then transferred to machine grinding device for homogenous mixing about an hour. Finally, the polycrystalline $Ba_2Bi^{3+}Bi^{5+}_{1-2x}Sb^{5+}_{2x}O_6$(x=0, 0.1, 0.2, 0.3,0.4, and 0.5) powder samples were obtained under heat treatment at 700-800^0 C for 24 hours.

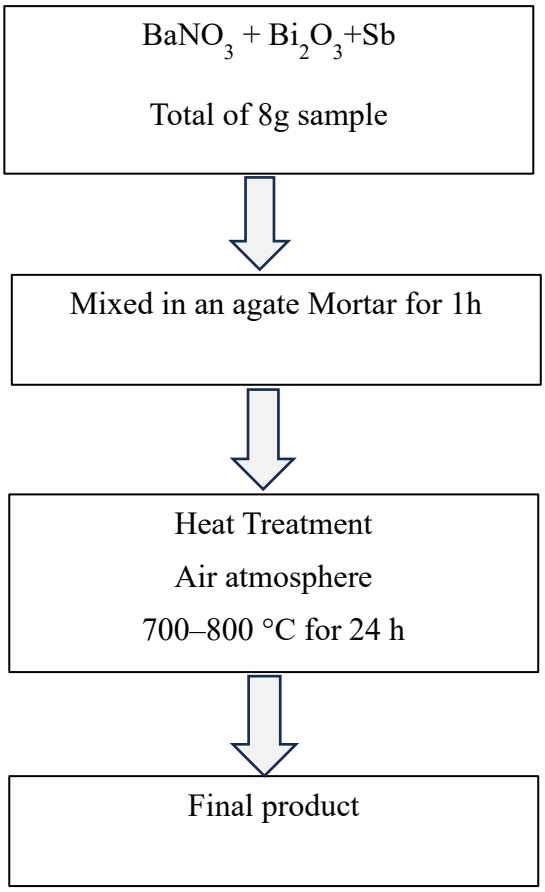

Figure 2.2: Solid-state synthesis flow chart diagram

2.2 Characterization

A. $Ba_2TbBi_{(1-x)}Sb_xO_6$

To study the crystallographic phase diagram of $Ba_2Tb(Bi,Sb)O_6$ by means of X-ray diffraction patterns the data were collected from a diffractometer (Ultima IV, Rigaku). Rietveld refinement FP-RIETAN program [27] were adopted to this research to obtained the crystal related details information like lattice parameters, atomic position, and other

parameters, listed in Table 1. Powder samples' surface area was calculated using BET analysis of N_2 absorption at 77 K (BELSORPmini II, Microtrac). The particle size distribution properties of $Ba_2Tb(Bi_{1-x}Sb_x)O_6$ polycrystalline samples were determined from scanning electron microspore (SEM) images. In this process, a film sample from powder $Ba_2Tb(Bi_{1-x}Sb_x)O_6$ fabricated through electrophoretic deposition technique (EPD) [28] to obtain clear SEM images. Optical properties were measured through Band gap estimation data following Kubelka-Munk function [17, 20, 22]. In the Kubelka-Munk equation of absorption coefficient, the required diffuse reflectance data were collected from a spectroscopy device (V550, JASCO Co.). Finally, the band gap energies were calculated from the extrapolation of absorption coefficient vs photon energy curve. Moreover, to study the Sb substitution effect in electronic properties theoretical investigation of density functional theory implemented 'Quantum ESPRESSO' package was applied [29, 30]. In this calculation, to estimate the exchange-correlation effect, Perdew–Burke–Ernzerhof (PBE) functional [31] scheme was applied. The fundamental electrical states were represented using pseudopotentials from the 'pslibrary' [32]. Monkhorst–Pack grid of 4×4×4 with cut off energy 40 Ry were employed for K-point sampling.

Next, to examine the Tb-ions ratio (trivalent and tetravalent state) in the present $Ba_2Tb(Bi_{1-x}Sb_x)O_6$ compounds, magnetic measurement was carried out using a superconducting quantum interference device magnetometer (MPMS, Quantum Design). From this experiment, temperature dependence dc magnetization susceptibility data were collected in colling process under the applied magnetic field of 0.1 T. Applying Curie–Weiss law, the effective magnetic moment values were calculated from the susceptibility data. Here, it is mentioned that the effective magnetic moment calculated for each $Ba_2Tb(Bi_{1-x}Sb_x)O_6$ compound represent the Tb ion's magnetic moments as only Tb is magnetic in the whole compound.

B. $Ba_2Bi^{3+}Bi^{5+}_{1-2x}Sb^{5+}_{2x}O_6$

X-ray diffraction patterns were obtained from a high-resolution multifunctional X-ray diffractometer (SmartLab 3G, Rigaku, Tohoku Univ.). The crystallographic phase purity of the powder $Ba_2Bi^{3+}Bi^{5+}_{1-2x}Sb^{5+}_{2x}O_6$ samples are analyzed through well fitted X-ray diffraction patterns using FP-RIETAN program [27]. The quality of fitness was ensured from the optimization of reliability factors, as shown in Figure 3.5 and Table 4. Structural related parameters are also obtained from Rietveld refinement analysis of fitted data, as displayed in Tables 3, 5, 6, and 7. Following the same experimental procedure of $Ba_2Tb(Bi,Sb)O_6$ as mentioned in the earlier section, SEM images and optical properties as well as band gap energy [17, 20, 22] of $Ba_2Bi^{3+}Bi^{5+}_{1-2x}Sb^{5+}_{2x}O_6$ were measured. Next, to investigate the Sb substitution effect in the electronic structure of $Ba_2Bi^{3+}Bi^{5+}_{1-2x}Sb^{5+}_{2x}O_6$ samples, density functional theory implemented Quantum ESPRESSO was conducted [33, 34]. For the exchange correlation, hybrid functional Heyd–Scuseria–Ernzerhof (HSE06) [35, 36] are adopted. The computation was performed using WANNIER90 package [37], [38], [39], [40]. For the Brillouin zone sampling, 4 × 4 × 4 Monkhorst–Pack grid through the cut-off energy 40 Ry is used to this calculation.

2.3 Photocatalytic activity measurement

A. MB degradation

Photocatalytic properties of powder $Ba_2Tb(Bi_{1-x}Sb_x)O_6$ and $Ba_2Bi^{3+}Bi^{5+}_{1-2x}Sb^{5+}_{2x}O_6$ samples as a catalyst was examined through the methylene blue dye (MB) degradation performances under visible light illumination [24]. The experimental set up for graphical representation are displayed in Figure 2.3. A 300 W Xenon lamp was considered as a light source, while only visible light incident to the target was ensured by placing two cut-of filters (UV and IR, Cermax LX300F, Excelitas Technologies) in front of the source. Next, a glass beaker containing 50 ml of 10 ppm MB dyes with 0.2 g of powder catalyst

was placed in a dark condition about 30 minutes under vigorous stirring to finalized the absorption desorption process. Finally, it transferred for visible light irradiation reductive MB degradation. The degradation of MB understands through the decolorization of aqueous MB into colorless leuco-MB under reduction process [41, 42]. This is a common property of MB and used widely for photocatalytic measurement purpose. The bleaching of MB with the presence of catalyst under electromagnetic radiation was measured from the UV–Vis spectrometer (V730, JASCO Co.). Every 30 minutes interval of 210 minutes, 3 mL from the main solution was taken for the MB degradation measurement into the test cell.

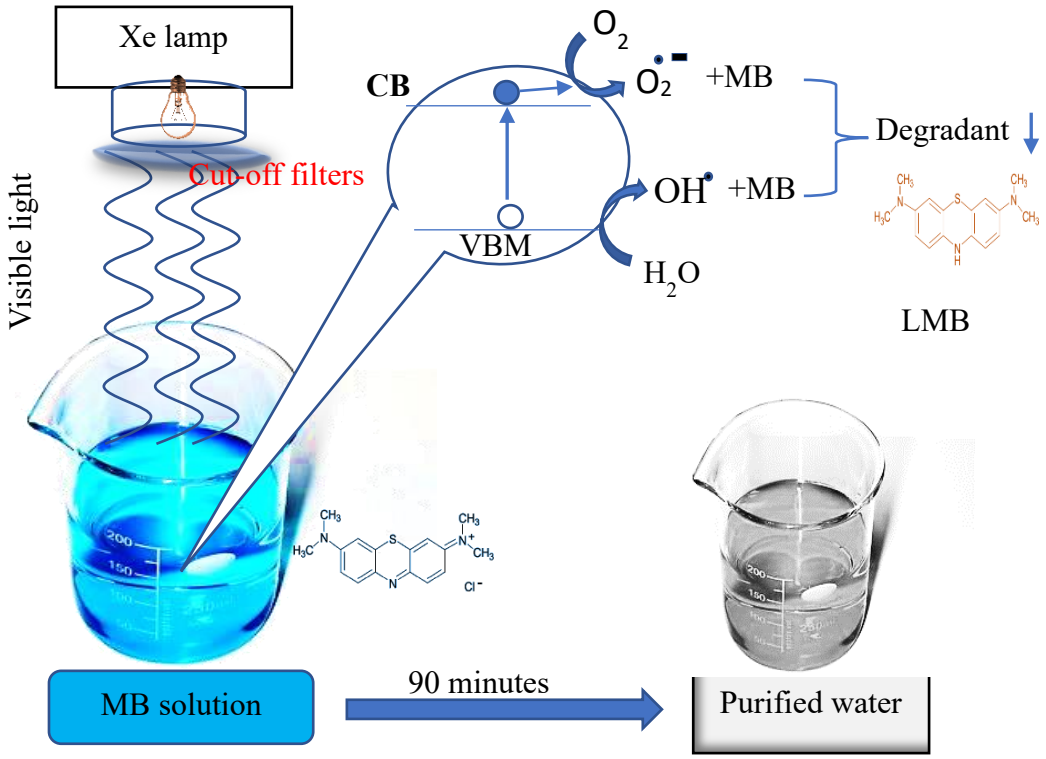

Figure 2.3: Graphical representation of Photocatalytic MB degradation experimental arrangement

B. IPA decomposition

Next to MB degradation, photocatalytic gaseous 2-propanol (IPA) decomposition was conducted, in order to make comparison. In this experiment, IPA was injected into a glass reactor containing $Ba_2Tb(Bi_{1-x}Sb_x)O_6$ or $Ba_2Bi^{3+}Bi^{5+}_{1-2x}Sb^{5+}_{2x}O_6$ powder catalyst. After that, the reactor was placed under visible light illumination. In Figure 2.4, the photocatalytic IPA decomposition catalytic reaction mechanism has been made for graphical demonstration. The oxidation of IPA decomposition took place on the surface of powder catalyst, resulted in CO_2 evolution. Using a Gas chromatograph device CO_2 concentration were detected and recorded in a regular time interval [22, 35].

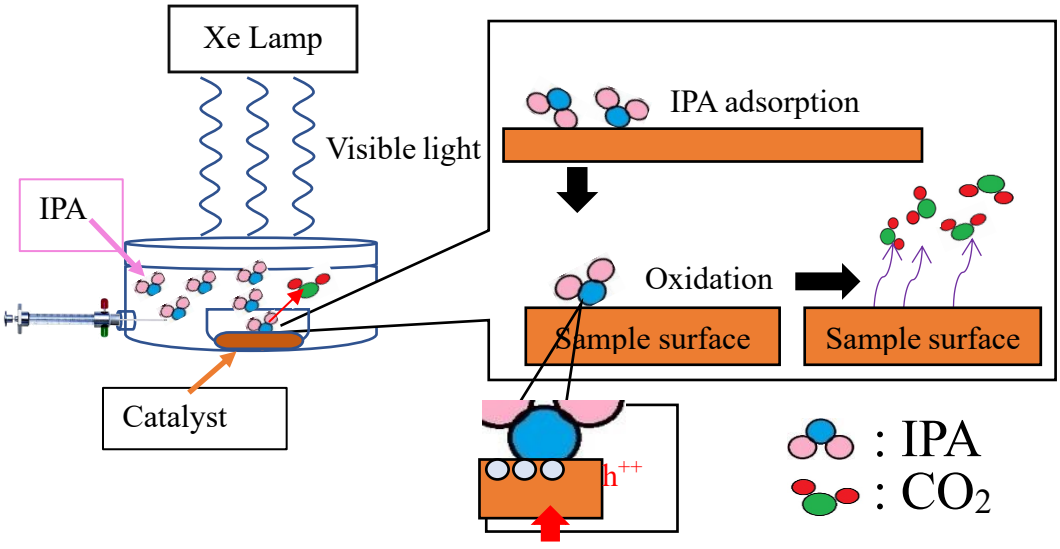

Figure 2.4: Photocatalytic IPA decomposition mechanism

Chapter 3

Results and Discussion

3.1 Structural Analysis

A. $Ba_2TbBi_{(1-x)}Sb_xO_6$

The crystallographic phase purity of the as-prepared powder samples synthesized by citrate technique was carried out from X-ray diffraction (XRD) analysis. Rigaku (Ultima UV) diffractometer were used to collect the diffraction related patterns of polycrystalline $Ba_2Tb(Bi,Sb)O_6$ samples. Figure 3.1 revealed the obtained XRD patterns for all $Ba_2Tb(Bi_{1-x}Sb_x)O_6$ samples, ranging from (Sb)x=0 to 1.0. In the lower Sb (x=0.0 and 0.1) samples, the peaks obtained for both compounds are found to be symmetric and well matched with the monoclinic crystal structure, can be crystalized in a monoclinic phase, confirmed from the literature review [25]. On the other hand, for higher Sb($0.5 \leq x \leq 1.0$) values, the samples are well crystalized in a cubic crystal structure. Crystal phase changes properties for $Ba_2Pr(Bi,Sb)O_6$ is observed at a certain concentration Sb(x)=0.5. The effect of Sb substitution on phase transition (monoclinic to cubic) at a particular concentration (x=0.5) was previously observed in Pr-based $Ba_2Pr(Bi,Sb)O_6$ double perovskite compounds [22]. This indicates the consistency of the present research with similar work and Sb(x)=0.5 can be considered as a critical point for Ba_2(Pr,Tb)$(Bi,Sb)O_6$ double perovskite oxide. Furthermore, to obtain all crystal related information, the data was fitted in Rietveld refinement using FP RIETAN program. Table 1 and Table 2 list the obtained structural parameters and their changes upon Sb substitution in $Ba_2Tb(Bi_{1-x}Sb_x)O_6$ double perovskite oxide. Previously reported lattice parameters (for x=1.0) strongly supported these obtained data [23, 30]. In Figure 3.2, the changes in lattice parameters as well as structural phase under Sb substitutions are plotted. The figure shows monotonic decreases in lattice parameters over Sb incorporation.

Table 1 Crystal structure and lattice parameters of $Ba_2Tb(Bi_{1-x}Sb_x)O_6$ as a function of Sb

Sb(*x*)	Crystal symmetry	*a* (Å)	*b*(Å)	*c*(Å)
0.0	Monoclinic	6.1223	6.0903	8.6110
0.1	Monoclinic	6.1069	6.0809	8.5916
0.5	Cubic	8.4814	8.4814	8.4814
0.6	Cubic	8.4611	8.4611	8.4611
1.0	Cubic	8.4506	8.4506	8.4506
$BaBiO_3$[14]	Monoclinic	6.1910	6.1407	8.6780

Table 2 Wyckoff positions and atomic coordinates of $Ba_2Tb(Bi_{1-x}Sb_x)O_6$ for x=0.0 and 1.0 compounds

For Sb(x)=0.0, Ba_2TbBiO_6 (monoclinic *I*/2*m* phase)				
atom	Wyckoff positions	*x*	*y*	*z*
Ba	4i	0.5036	0.5	0.25
Tb	2c	0.5	0	0
Bi	2b	0	0.5	0
O1	8j	0.24210	0.25400	-0.03340
O2	4i	0.43610	0	0.25890
For Sb(x)=0.0, Ba_2TbSbO_6 (cubic $Fm\bar{3}m$ phase)				
Ba	8c	0.25	0.25	0.25
Tb	4b	0.5	0.5	0.5
Sb	4a	0	0	0
O	24e	0.237	0	0

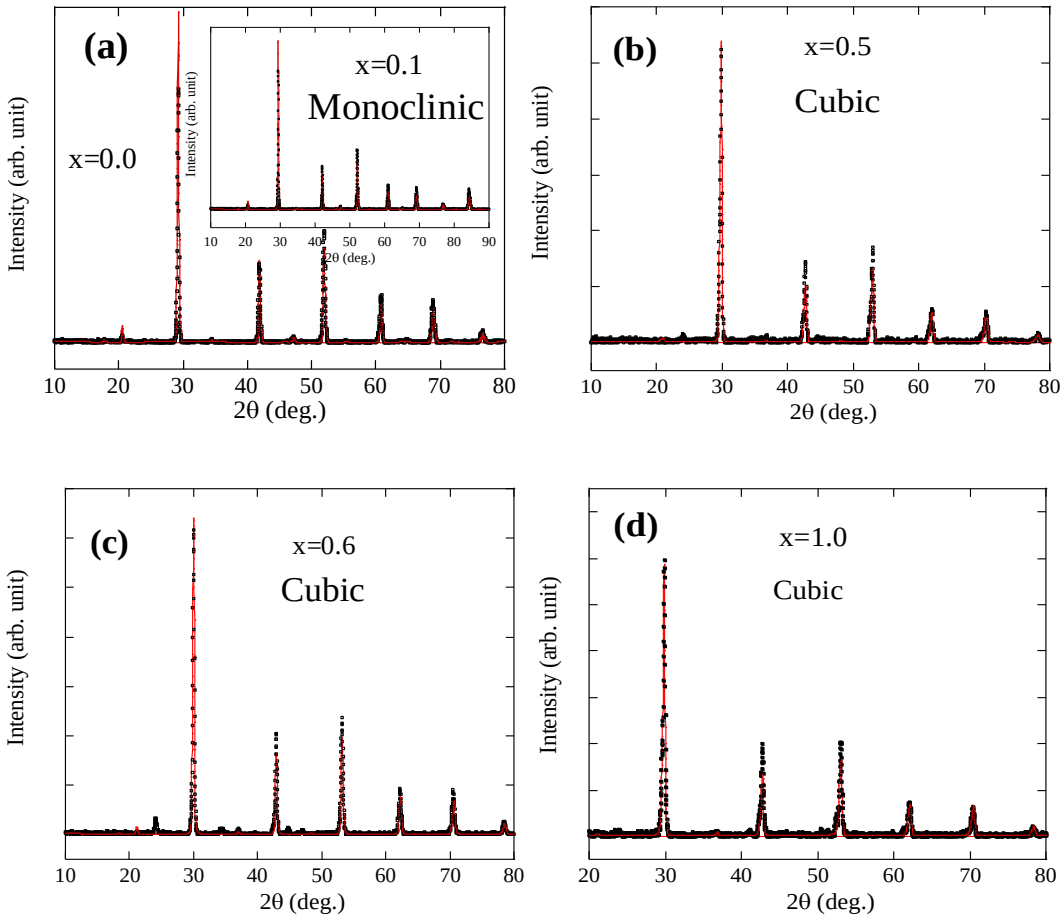

Figure 3.1: X-ray diffraction patterns of $Ba_2Tb(Bi_{1-x}Sb_x)O_6$ for (a) x=0.0 and 0.1 (inset), (b) x=0.5, (c) x=0.6, and (d) x=1.0. The black dots represent experimental data and Rietveld refinement data are represented by red color line

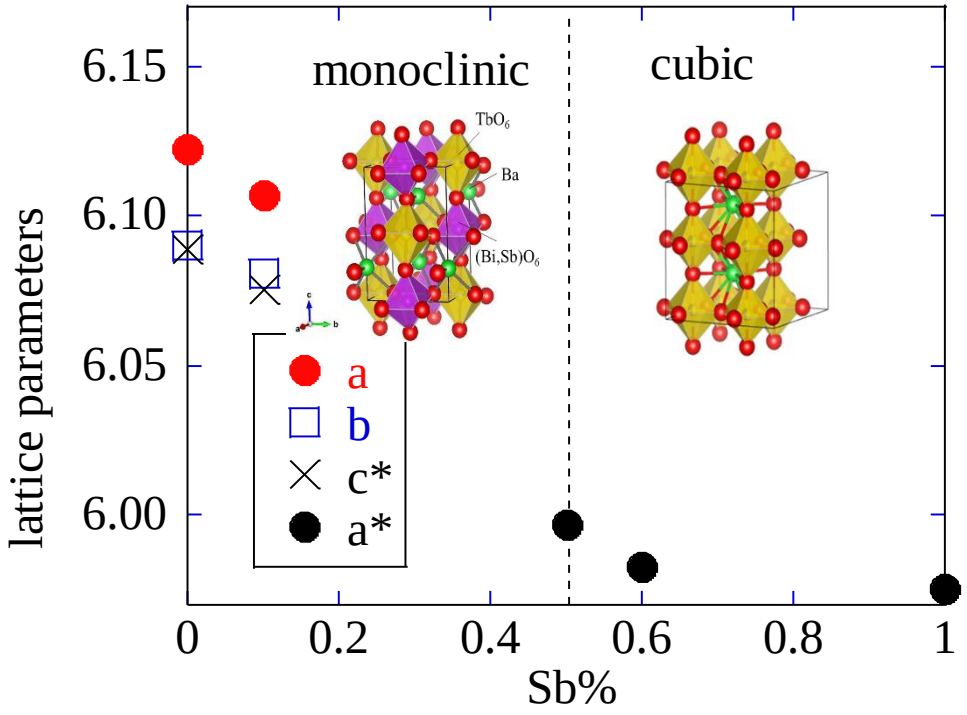

Figure 3.2: Lattice parameters of $Ba_2Tb(Bi_{1-x}Sb_x)O_6$ as function of Sb (x=0.0, 0.1, 0.5, 0.6, and 1.0). a^* ($a^* = a/\sqrt{2}$) and c^*($c^* = c/\sqrt{2}$) represents the reciprocal of *a* and *b* lattice parameters

B. $\mathbf{Ba_2Bi^{3+}Bi^{5+}_{1-2x}Sb^{5+}_{2x}O_6}$

The phase purity of the polycrystalline powder $Ba_2Bi^{3+}Bi^{5+}_{1-2x}Sb^{5+}_{2x}O_6$(x=0, 0.1, 0.2, 0.3, 0.4, and 0.5) samples are made from the X-ray diffraction pattern analysis. To obtain precise structural information, X-ray data are collected from a high resolution based multifunctionalized SmartLab 3G (Rigaku) diffractometer. Figure 3.3 illustrates the X-ray data of the prepared samples, revealed the formation of monoclinic (with *I*2*m* phase) in the x values from 0 to 0.4 and rhombohedral (with $R\bar{3}$ phase) for x=0.5. According to the literature review, these data are good agreement to the formation of monoclinic and

rhombohedral phases. For instance, the monoclinic phase has been detected according to the previous reports [44, 45]. In case of x=0.5, the formation of rhombohedral phase confirmed from the previous research [46]. The presence of impurity phases with the main phase for the partial Sb (x= 0.1, 0.2, 0.3, and 0.4) substitution is a common property, reported in former researches [47]. The generation of excessive Sb^{5+} during the sample preparation may lead to the formation of these extra phases. However, in this present research, successfully achieved single phase monoclinic structure. It is expected that unique sample preparation technique may reflected to this result. Nevertheless, the assigned peaks as marked in asterisk sign (*) in case of x=0.3 and 0.4 are responsible for $R\bar{3}$ phase phase, reported by Yasukawa et al. [48]. The lattice parameters obtained from the X-ray data analysis are depicted in Table 3. For the parent compound, these values are found to be a = 6.1964(2) Å, b = 6.1506(1) Å, and c = 8.6857(3) Å. The substitution of smaller Sb^{5+} (0.60 Å) in place of Bi^{5+}(0.76 Å) resulted in a lattice parameter decrement as well as cell volume contraction. In Figure 3.4, the change of lattice parameters as a function of Sb is demonstrated, which indicates a monotonic decrease behavior. Neutron diffraction pattern analysis of Rietveld refinement data in the earlier research ensured the placement of Sb^{5+} at Bi^{5+} position [45, 49].

Table 3 Sb dependent crystal phase, lattice parameters, and unit cell volume of $Ba_2Bi^{3+}Bi^{5+}_{1-2x}Sb^{5+}_{2x}O_6$

Sb x	Space group	*a* (Å)	*b* (Å)	*c* (Å)	α (º)	β (º)	V ($Å^3$)
0.0	*I*2/*m*	6.1964(2)	6.1506(1)	8.6857(3)	90	90.180(2)	331.03(1)
0.1	*I*2/*m*	6.1843(4)	6.1417(1)	8.6800(6)	90	90.117(4)	329.68(4)
0.2	*I*2/*m*	6.1354(11)	6.1331(9)	8.686(2)	90	90.25(1)	326.83(1)
0.3	*I*2/*m*	6.1035(8)	6.1182(5)	8.652(1)	90	90.436(7)	323.09(7)
0.4	*I*2/*m*	6.0965(4)	6.0806(3)	8.6529(6)	90	90.443(3)	320.77(3)
0.5	$R\bar{3}$	6.0575(2)	6.0575(2)	6.0575(2)	60.126(1)	60.126(1)	315.24(2)

Table 4 FP-RIETAN program utilized optimized R-factor parameters for different Sb values

Sb x	Crystal phase	R_{WP} (%)	R_P (%)	R_B (%)
0.0	Monoclinic(*I*2/*m*)	8.95	6.32	2.93
0.1	Monoclinic(*I*2/*m*)	7.20	4.86	2.99
0.2	Monoclinic(*I*2/*m*)	11.56	8.50	2.96
0.3	Monoclinic(*I*2/*m*)	9.84	7.09	3.05
0.4	Monoclinic(*I*2/*m*)	8.72	6.11	3.33
0.5	Rhombohedral($R\bar{3}$)	9.50	6.18	2.95

Table 5 Estimated bond lengths and bond angles for $Ba_2Bi^{3+}Bi^{5+}_{1-2x}Sb^{5+}_{2x}O_6$

Sb x	Bond lengths (Å)				Bond angles (°)	
	Bi(1)-O(1)	Bi(1)-O(2)	Bi(2)/Sb-O(1)	Bi(2)/Sb-O(2)	Bi(1)-O(1)-Bi(2)/Sb	Bi(1)-O(2)-Bi(2)/Sb
0.0	2.29(2)	2.260(4)	2.12(2)	2.160(8)	160.4(8)	162.0(6)
0.1	2.29(2	2.302(6)	2.12(2)	2.080(9)	160.5(7)	168.0(7)
0.2	2.34(4)	2.29(1)	2.08(3)	2.07(2)	158(1)	168(1)
0.3	2.29(2)	2.30(1)	2.10(2)	2.03(1)	160.2(8)	170.1(9)
0.4	2.29(3)	2.35(1)	2.05(3)	1.95(2)	172(2)	172.2(4)
x	Bi-O		Sb-O		Bi-O-Sb	
0.5	2.323(6)		1.983(6)		169.3(3)	

Rietveld refinement FP-RIETAN program is performed to collect the crystallographic phase related other structural parameters. All the estimated parameters including lattice parameters, cell volume, bond lengths, bond angles, and Wyckoff positions are depicted in Tables 3, 4, 5, 6 and 7. It is worth noted that a clear crystallographic point view can be

made from the perfect fitting of XRD patterns. Here, the quality of fitness carefully measured from the reliability factor (R) optimization, considering negligible difference between experimental and calculated data. The detailed of Rietveld refinement XRD patterns are delineated in Figure 3.5. For all samples, the values of R factors are maintained at R_{wp} = 7.20 ~ 11.56, Rp = 4.86 ~ 8.50, and R_B = 2.93 ~ 3.33, indicates good fitness. Table 4 listed the fitting related parameters with the corresponding crystal phases. The bond length and bond angles of the constituent atoms in the present $Ba_2Bi^{3+}Bi^{5+}_{1-2x}Sb^{5+}_{2x}O_6$ compounds are estimated and displayed in Table 5. Here, different bond lengths for Bi/Sb with oxygen represents the ionic states of Bi and Sb and types of adjacent oxygen atom in the octahedral junction making the crystal. Although, in the present investigation observed a single bond of pentavalent of state of Sb, as described above. However, comparatively lower and higher bond lengths for Bi(1)-O and Bi(2)-O in Table 5 are reasonable for pentavalent (Bi^{5+}) and trivalent (Bi^{3+}) lower ionic states of Bi. The result comprises strong covalent nature for Bi^{5+} significantly attract the O atom closer than Bi^{3+} and reduces the interatomic distance. It is a common property for mixed valence states.

Table 6 Atomic Wyckoff positions and fractional coordinates for the monoclinic $Ba_2Bi^{3+}Bi^{5+}_{1-2x}Sb^{5+}_{2x}O_6$ (x=0 to 0.4) phases

$Ba_2Bi^{3+}Bi^{5+}_{1-2x}Sb^{5+}_{2x}O_6$ Atom (x=0, 0.25, 0.5)	*I*2/*m* site	*x*	*y*	*z*
Ba	4*i*	0.5029	0	0.2487
Bi1	2*a*	0	0	0
(Bi2, Sb)	2*d*	0	0	0.5
O2	8*j*	0.2611	0.2574	-0.0327
O1	4*i*	0.0606	0	0.2604

Table 7 Atomic Wyckoff positions and fractional coordinates for the rhombohedral $Ba_2Bi^{3+}Bi^{5+}_{1-2x}Sb^{5+}_{2x}O_6$ (x=0.5) phase

$Ba_2Bi^{3+}Sb^{5+}O_6$ Atom (x=0.5)	*I*2/*m* site	*x*	*y*	*z*
Ba	2*c*	0.2566	0.2566	0.2566
Bi	1*a*	0	0	0
Sb	1*b*	0.5	0.5	0.5
O2	6*f*	0.2319	0.2984	0.7271

Moreover, lowering the bond length due to Sb substitution is the reason for small ionic size of Sb^{5+} (0.60 Å). According to previously reported average bond lengths of 2.29 Å (for Bi^{3+}-O) and 2.12 (for Bi^{5+}-O) for the parent compounds from neutron diffraction analysis [50], present estimation shows good agreement. The octahedral tilting due to charge compensation in crystals lattice responsible for structural distortion plays important role in the physical properties of a solids can be understand through bond angles.

The effect of Sb substitution on structural distortion of $Ba_2Bi^{3+}Bi^{5+}_{1-2x}Sb^{5+}_{2x}O_6$ double perovskite oxide in terms of bond angle is calculated which is displayed in Table 5. Furthermore, to obtain insight of the crystal structure, the crystallinity for the $Ba_2Bi^{3+}Bi^{5+}_{1-2x}Sb^{5+}_{2x}O_6$(x=0, 0.1, 0.2, 0.3, 0.4, and 0.5) samples are estimated in terms of crystallite size. Following Williamson-Hall method, the crystallite sizes as a function of Sb concentration are calculated using FP-RIETAN program. In the whole range of x (0 to 0.5), the crystallite sizes are found to be 70 nm, 65 nm, 132 nm, 135 nm, 52 nm, and 49 nm, as shown in Table 8. It is obvious that high crystallinity observed for Sb substituted samples.

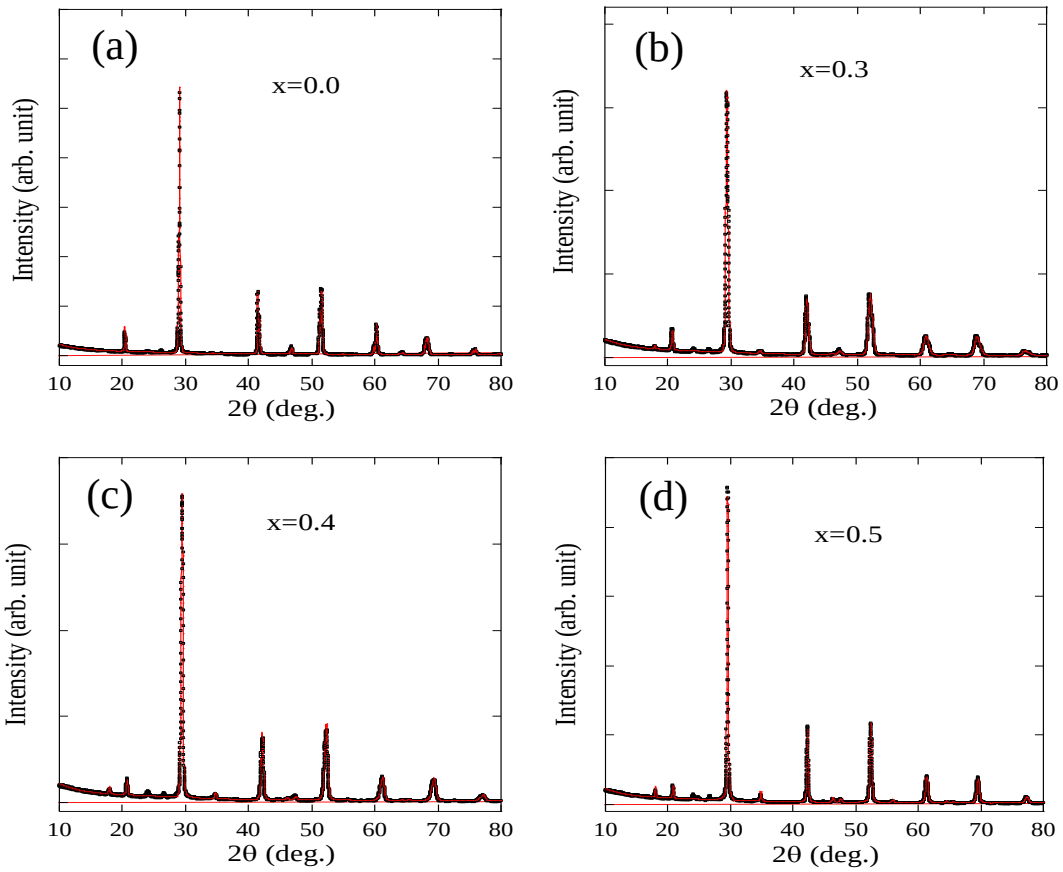

Figure 3.3: X-ray diffraction pattern of $Ba_2Bi^{3+}Bi^{5+}_{1-2x}Sb^{5+}_{2x}O_6$ for (a) x=0.0, (b) x=0.03, (c) x=0.4, and (d) x=0.5. The black dots and solid red lines represent the experimental and refined data, respectively. For refinement FP-RIETAN program are used

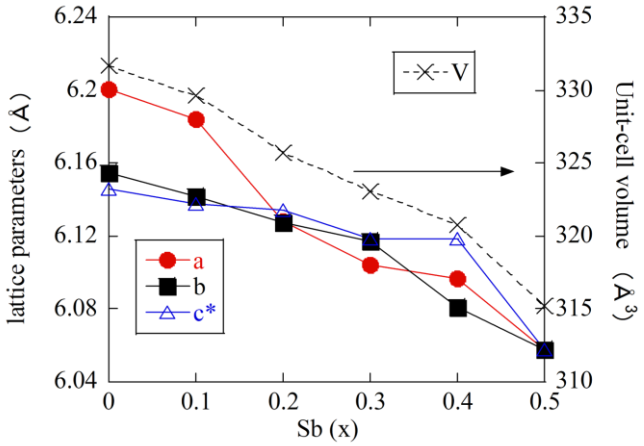

Figure 3.4: Lattice parameters (left-hand side) and Unit cell volume (right hand side) of $Ba_2Bi^{3+}Bi^{5+}_{1-2x}Sb^{5+}_{2x}O_6$ perovskite as a function of Sb. ($c^* = c\sqrt{2}$)

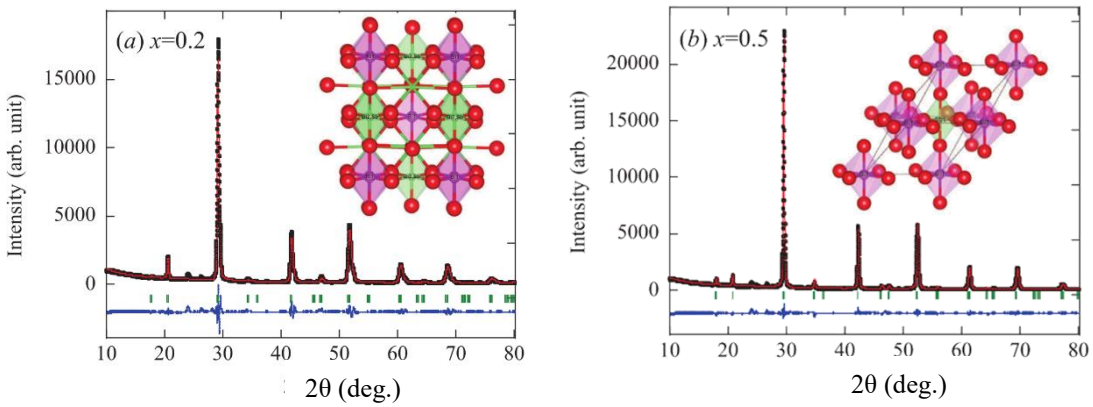

Figure 3.5: FP-RIETAN program used refined XRD data of $Ba_2Bi^{3+}Bi^{5+}_{1-2x}Sb^{5+}_{2x}O_6$ for (a) x=0.2 and (b) x=0.5. Experimentally obtained black dotted data are fitted with solid red line. The solid blue color line at the bottom represents the difference between experimental and calculated curves where the intermediate tick marks Bragg reflection position

3.2 Magnetic measurement

A. $Ba_2TbBi_{(1-x)}Sb_xO_6$

Next to understand the valence state of Tb ion and its changes in terms of Sb concentration, magnetic susceptibility data was determined from a SQUID magnetometer device. Using Curie-Weiss law of effective magnetic moment (μ_{eff}) calculation formula [22], the μ_{eff} value for each compound is then estimated from the magnetic susceptibility data. The estimated values of μ_{eff} are effectively 8.98 μ_B, 8.89 μ_B, 8.86 μ_B, and 9.13 μ_B respectively, for x = 0, 0.1, 0.5, and 0.6 samples. Figure 3.6 (a) illustrates the calculated effective magnetic moment of $Ba_2Tb(Bi_{1-x}Sb_x)O_6$ compounds. Theoretically estimated magnetic moment values of $Tb^{3+}(\mu_{eff} = 9.72\ \mu_B)$ and $Tb^{4+}(\mu_{eff} = 7.94\ \mu_B)$ are also included in Figure 3.6(a) (top dash-dot line and bottom black line).

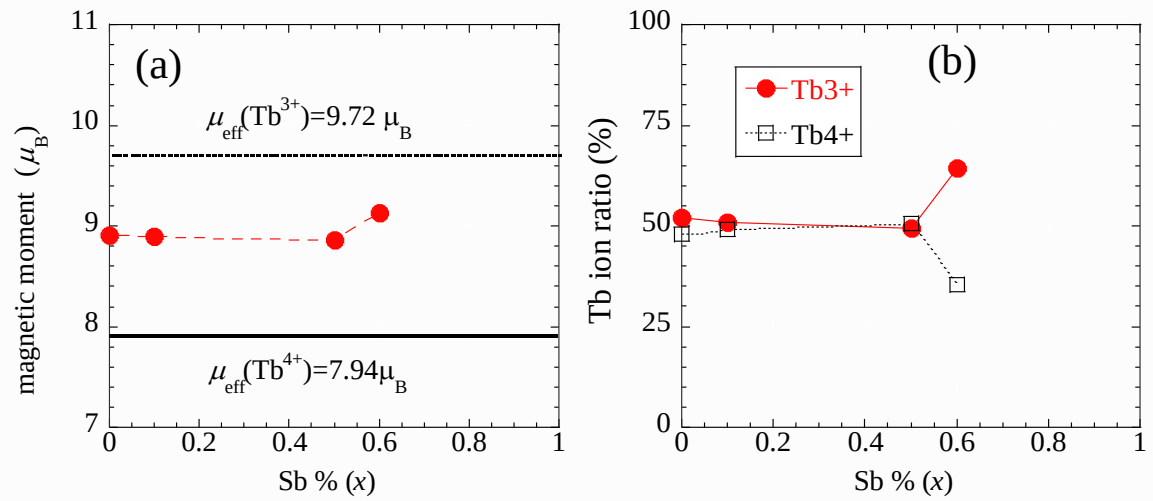

Figure 3.6: (a) Calculated effective magnetic moment and (b) Estimated ratio of Tb^{3+} and Tb^{4+} for $Ba_2Tb(Bi,Sb)O_6$ double perovskite. Data obtained from magnetic susceptibility measurement not shown in here. $Tb^{3+}(\mu_{eff} = 9.72\ \mu_B)$ and $Tb^{4+}(\mu_{eff} = 7.94\ \mu_B)$ are known values

It is obvious from Figure 3.6 (a) that the calculated effective magnetic moment value stands in the intermediate between Tb^{3+} and Tb^{4+} magnetic moments, referring to the possibility of mixed valence state. For confirmation, the ratio of Tb^{3+} and Tb^{4+} ions can be calculated following the formula [22, 52] of effective magnetic moment,

$$\mu_{eff}^2 = y\mu_{eff}^2(Tb^{3+}) + (1-y)\mu_{eff}^2(Tb^{4+}) \qquad \text{Equ. (1)}$$

Where y and (1-y) represents the percentages of Tb^{3+} and Tb^{4+} ions respectively.

The calculated ratio of Tb^{3+} and Tb^{4+} and corresponding effective magnetic moment data are displayed in Table 8. It is observed that the ratio of Tb^{3+} and Tb^{4+} changes significantly with Sb concentrations and is found to be 0.51:49 to 0.64:0.36 from x = 0.1 to 0.6. Furthermore, the values are plotted as a function of Sb content to see their variations over the whole sample and are depicted in Figure 3.6 (b). It can be seen that the Tb^{3+} amount considerably increases with Sb values compared to Tb^{4+}. This finding confirms the presence of mixed valence states of Tb ions in the present examine $Ba_2Tb(Bi_{1-x}Sb_x)O_6$ double perovskite. The properties indicate a common characteristic of rare based double perovskite which has been previously observed in different rare earth double perovskite [22]. Further support is provided by the observation of a shoulder structure of the tetravalent ion accompanied by a dominant peak of the trivalent ion on the Pr-based sample as determined by an X-ray photoemission spectroscope [53].

Table 8 Effective magnetic moment and ratio of Tb ion in $Ba_2Tb(Bi,Sb)O_6$ [$\mu_{eff}(Tb^{3+}) = 9.72\ \mu_B$, $\mu_{eff}(Tb^{3+}) = 7.94\ \mu_B$]

Sb(x)	0.0	0.1	0.5	0.6
$\mu_{eff}(\mu_B)$	8.91	8.89	8.86	9.13
Tb^{3+}: Tb^{4+}	0.52:0.48	0.51:0.49	0.49:0.51	0.64:0.36

3.3 Phase stability calculation

A. $Ba_2TbBi_{(1-x)}Sb_xO_6$

A polycrystalline solid material's physical properties are largely affected by the structural stability factor [7]. In this research, the phase stability of $Ba_2Tb(Bi_{1-x}Sb_x)O_6$ double perovskite oxide is explained by means of tolerance factor estimation. It is possible to measure lattice distortion in ABO_3 perovskite as it has a direct connection with the tolerance factor. Under proper charge consideration, an accurate picture of crystallographic phase can be identified through tolerance estimations. Considering the mixed valence of Tb ions as ensured in the earlier section of magnetic measurement, the tolerance factor values can be calculated using the formula,

$$t = \frac{r_{Ba}+r_O}{\sqrt{2}(\frac{r_{Tb}+r_M}{2}+r_O)} \qquad \text{Equ. (2)}$$

Where r_{Ba} , r_O, r_{Tb}, and $r_{M=(Bi,Sb)}$ are the respective ionic radii of the constituent atoms [54]. In the calculation process, few attempts has been made to describe the chemical formula constituting particular ionic states formed $Ba_2Tb(Bi_{1-x}Sb_x)O_6$ double perovskite oxide. All probable ionic states that may appear in the studied compound are considerably accounted to this research. In the first step, considering mixed valence state of Tb, the chemical formula can be evaluated as $Ba_2^{2+}Tb_{0.5}^{3+}Tb_{0.5}^{4+}Bi_{(1-x)/2}^{5+}Sb_{x/2}^{5+}M1_{(1-x)/2}^{4+}M2_{x/2}^{4+}O_6$ where $M1^{4+}$ and $M2^{4+}$ set as $M1^{4+} = Bi_{0.5}^{3+}Bi_{0.5}^{5+}$, and $M2^{4+} = Sb_{0.5}^{3+}Sb_{0.5}^{5+}$, respectively [25]. Next, considering the individual (trivalent and tetravalent) ionic state of Tb in $Ba_2Tb(Bi_{1-x}Sb_x)O_6$. Although, there is no possibility of single valence according to the experimental analysis. However, for further confirmation and in order to check the reliability of this investigation estimated the tolerance factor data points with the chemical formula $Ba_2^{2+}Tb^{3+}Bi_{1-x}^{5+}Sb_x^{5+}O_6$ and $Ba_2^{2+}Tb^{4+}M1_{1-x}^{4+}M2_x^{4+}O_6$. The

estimated values of tolerance factor for all three cases are listed in Table 9. In addition, the data are also plotted as a function of Sb for crystallographic representation, and shown in Figure 3.7. Depending on the t values, Figure 3.7 can be divided in three separated regions on the view point of monoclinic, rhombohedral, and cubic phase, respectively. The tolerance factor for $Ba_2Ln(Bi, Sb)O_6$ as a function of the ionic radius of Ln (Ln: rare-earth element) has been reported in previously [51]. Although, estimated tolerance factor values for all three cases well-supported by the reported data in lower Sb incorporated samples, confliction arises for higher Sb values. However, the data estimated for mixed valence states (red line in Figure 3.7) perfectly matched with the phases obtained in the entire Sb values.

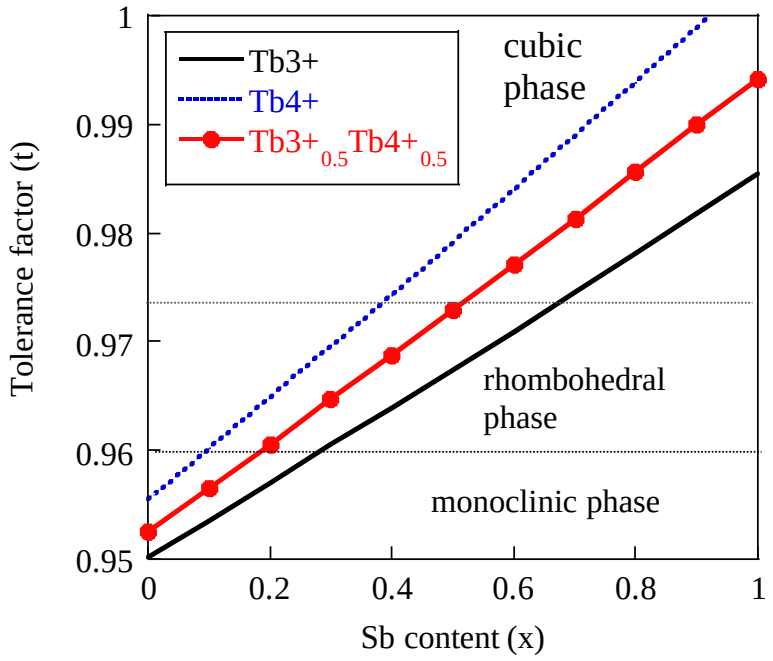

Figure 3.7: Tolerance factor estimation of $Ba_2Tb(Bi_{1-x}Sb_x)O_6$ as a function of Sb

The results show a clear relation of ionic states dependent phase stability measurement and confirm mixed phases ($Tb_{0.5}^{3+}Tb_{0.5}^{4+}$) in the studied $Ba_2Tb(Bi_{1-x}Sb_x)O_6$ compound. For x=0.5 sample, the estimated tolerance factor value t=0.973 which is just located on the boundary line of cubic phases represent the stability of cubic phases for higher Sb substitution [55]. The rise in t values for the higher contribution of Tb^{3+} and Tb^{4+} in responds to the Sb values towards unity indicates phase stability enhanced under Sb substitution [56]. Therefore, current investigation confirms the presence of Tb mixed valence state and support the magnetic analysis report.

B. $\mathbf{Ba_2Bi^{3+}Bi_{1-2x}^{5+}Sb_{2x}^{5+}O_6}$

The phase stability is an essential parameter for a catalyst to support its long-time photocatalytic activities. The phase stability can be measured through the tolerance factor estimation as its directly related to the crystal structure of a solid. In double perovskite the octahedral tilting due to many aspects especially cationic size mismatch reflected in the system towards structural distortion. In previous, Otsuka et al, explained the structural distortion as a function of ionic radii through tolerance factor calculation [57]. Here, the tolerance factor (t) values of $Ba_2Bi^{3+}Bi_{1-2x}^{5+}Sb_{2x}^{5+}O_6$ double perovskite are calculated with the different Sb(x) values. Following the same equation used in the earlier section for tolerance factor calculation, the formula of 't' can be written as

$$t = \frac{r_{Ba} + r_O}{\sqrt{2}\left(\frac{r_{Bi^{3+}} + r_{M^{5+}}}{2} + r_O\right)}$$

where r_{Ba}, $r_{Bi^{3+}}$, and $r_{M^{5+}(M=Bi,Sb)}$represent the ionic radii of the specific ions. These values are considered as $r_{Ba} = 1.61$ Å(Ba^{2+}), $r_{Bi^{3+}} = 1.03$ Å, $r_{Bi^{5+}} = 0.76$ Å, $r_{Sb^{5+}} = 0.60$ Å, and $r_{O^{2-}} = 1.4$ Å, respectively, in appropriate to the Shannon ionic radii [54]. Finally, the 't' values are calculated and listed in Table 9. The values are found to be increasing trend with Sb concentration towards unity, indicates the stability upon Sb substitutions.

Table 9 Crystallite size, tolerance factor, and crystal phase of $Ba_2Bi^{3+}Bi^{5+}_{1-2x}Sb^{5+}_{2x}O_6$ as a function of Sb

Sb x	Crystallite size (nm)	Tolerance factor	Crystal phase
0.0	70	0.927	Monoclinic
0.1	65	0.934	Monoclinic
0.2	132	0.941	Monoclinic
0.3	135	0.947	Monoclinic
0.4	52	0.954	Monoclinic
0.5	49	0.961	Rhombohedral

For the parent and end member compound, the estimated 't' values are found to be 0.927 in the monoclinic phase region and 0.96 in the rhombohedral phase boundary. According to the literature review, these values clearly support to the formation of monoclinic and rhombohedral phases. Furthermore, to demonstrate the effect of $B^{//}$-site ionic radii difference on crystal distortion, tolerance factor values of rare-earth based other double perovskite $Ba_2(Pr,Tb)(Bi,Sb)O_6$ are plotted along with the $Ba_2Bi^{3+}Bi^{5+}_{1-2x}Sb^{5+}_{2x}O_6$compound and delineated in Figure 3.8. The data showed a good relation of crystal phase formation with $B^{//}$-site ionic radii changes. The rise in 't' values observed for lower ionic radii in highly Sb substituted samples. In case of rare-earth based compound (Pr, Tb), the maximum values are obtained in the cubic region, while rhombohedral region for $Ba_2Bi^{3+}Sb^{5+}O_6$ compound. However, other compounds are found in the monoclinic region of lower ionic radii. The present investigation shows good relation with the previously reported data [57].

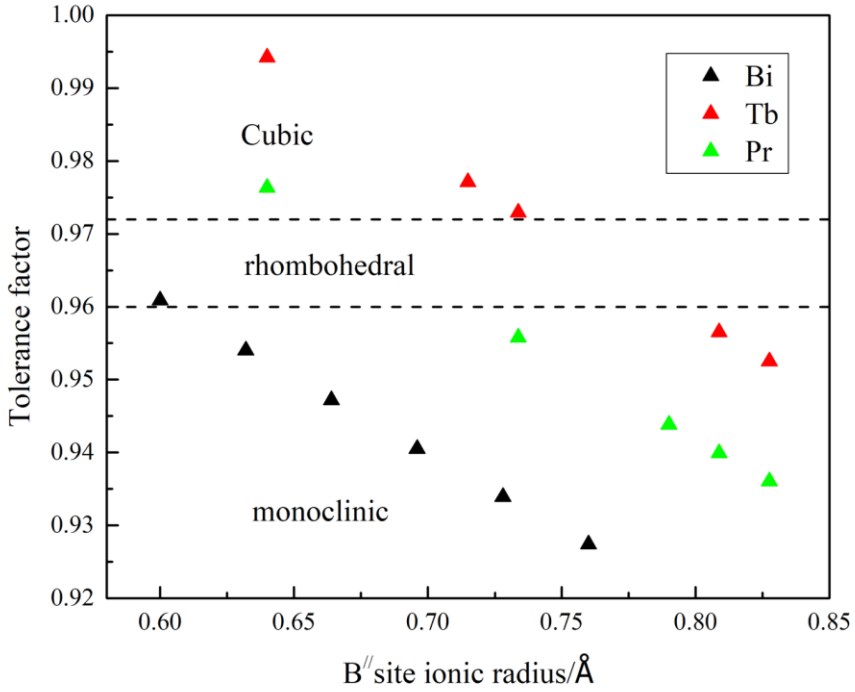

Figure 3.8: Tolerance factor of Ba_2(Bi, Pr,Tb)(Bi,Sb)O_6 as a function of ionic radius

3.4 B-site Order and Disorder structure analysis

A. $Ba_2TbBi_{(1-x)}Sb_xO_6$

B-site cation order and disorder structure is an important feature of $A_2BB'O_6$ double perovskite oxide. The intriguing properties can be determined depending on this arrangement of B-site cations in the $A_2BB'O_6$ structural phase. The case becomes a little more complex when more than two cations are placed in these two positions (BB′). In this

research, this order and disorder issue is studied with reasonable facts. At first, the case can be distinguished from X-ray diffraction patterns of $Ba_2Tb(Bi_{1-x}Sb_x)O_6$ by identifying a peak that corresponds to the Bragg position $2\theta=18^0$, responsible for order double perovskite [22]. Looking at Figure 3.9, no peak in particular can be seen at the angle ($2\theta=18^0$) in the whole range of Sb(x) indicates B-site cations are not well organized in $Ba_2Tb(Bi_{1-x}Sb_x)O_6$ phase. However, Rietveld refinement pattern, as shown in Figure 3.5 (inset), suggested the peak intensity at the concerned angles ($2\theta=18^0$) is a function of Sb concentration. The result indicates progression of disordering at higher Sb instead of complete disordering fact, means partial disordering effect. Another possible reason for low X-ray scattering power difference between Tb and Sb may be reflected in this disappearing phenomenon.

In the next, the phenomenon of order and disorder can be described through B-site cations size mismatch and charge differences. In general, B-site cations (B and $B^{/}$) ordering depends mostly on their ionic radius difference Δr_B, ($\Delta r_B = | r_B - r_{B^{/}} |$) and oxidation state difference ΔZ_B ($\Delta Z_B = | Z_B - Z_{B^{/}} |$). For order double perovskite, these values are maintained to be $\Delta r_B > 0.17$Å and $\Delta Z_B > 2$. In particular, for trivalent state of Tb i.e., $A_2^{2+}B^{3+}B^{/5+}O_6$ case $\Delta Z_B=2$ and tends to order structure with increasing $\Delta r_B (> 0.17)$ values [19]. For the tetravalent state of Tb i.e., $A_2^{2+}B^{4+}B^{/4+}O_6$ case, $\Delta Z_B=0$ and $\Delta r_B < 0.17$ suggested disorder structure double perovskite. It is clear from the above discussion that both the individual Tb^{3+} and Tb^{4+} cannot explain the ordering and disordering phenomena in relation to the experimental result. Therefore, we expected that the present mixed valence state of Tb would reflect a partially disordered phase.

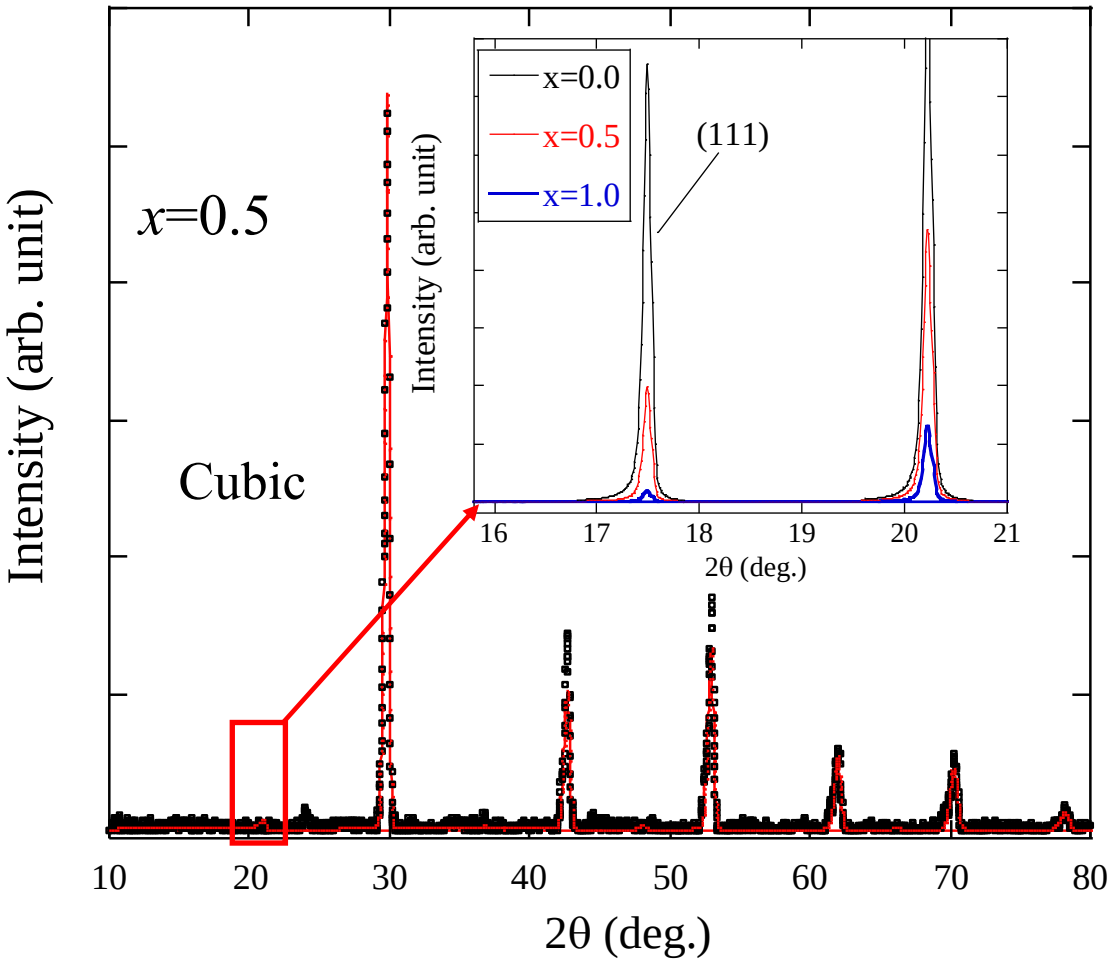

Figure 3.9: Least square fitted X-ray diffraction pattern for x=0.5. Inset shows only the calculated data (for x=0.0, 0.5, and 1.0), indicates the appearance of peak intensities as a function of Sb

3.5 SEM Analysis

A. $Ba_2TbBi_{(1-x)}Sb_xO_6$

Particle size distributed physical properties of $Ba_2Tb(Bi_{1-x}Sb_x)O_6$ as a function of Sb under citrate technique was evaluated from the SEM images analysis obtained from SEM device. The well-crystallized, uniformly distributed identical particles deposited electrophoretically on the film substrate are clearly represented in Figure 3.10.

In Figure 3.10 (a), SEM image of parent $Ba_2Tb(Bi, Sb)O_6$ compound is presented, collected from the previous research [25]. The ability to produce high quality powder samples using the citrate method has been proven for a long while and is utilized in many cases where sample quality is of the utmost importance.

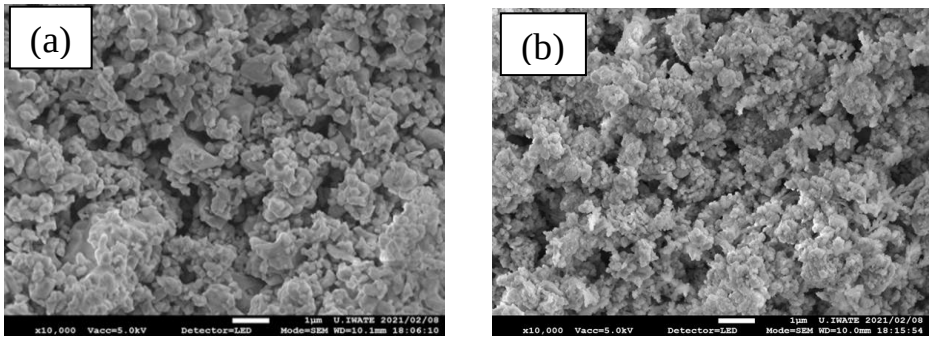

Figure 3.10: Particle size distribution SEM images of $Ba_2Tb(Bi_{1-x}Sb_x)O_6$ at (a) x=0.0 [25] and (b) 0.5

For example, in the preparation of $Ba_2Pr(Bi_{1-x}Sb_x)O_6$ double perovskite oxide, two different synthesis approach was considered [22]. In the first step, followed by citrate method average particle sizes were obtained in the order of 0.2-0.5 μm. However, it was at least one order higher than citrate when the same sample was prepared in conventional solid-state technique. Furthermore, the quality of particle size distributions was found to be enhanced remarkably while Sb was incorporated into Bi site. Accordingly, for the present case of $Ba_2Tb(Bi_{1-x}Sb_x)O_6$ samples, seen in the SEM photograph of Figure 3.10(b), the result is reflected in the Sb substituted compound. This enhancement in the quality of powder samples indicates Sb substitution at Bi site promotes the refinement of polycrystalline samples. In photocatalysis process, this refinement of powder samples is of great importance in the preparation of a unique photocatalyst.

B. $\mathbf{Ba_2Bi^{3+}Bi^{5+}_{1-2x}Sb^{5+}_{2x}O_6}$

The particle size distribution morphological analysis of solid state synthesized $Ba_2Bi^{3+}Bi^{5+}_{1-2x}Sb^{5+}_{2x}O_6$ samples are made from SEM images collected from scanning electron microscope equipment. Figure 3.11 represent the corresponding SEM images for parent, 20% Sb incorporated, and end member compound, respectively. It is obvious from Figure 3.11(a) that large crystallite sizes with irregularly distributed grains are formed in the parent sample, suggested poor crystallinity. However, literally smaller particles with improved morphology obtained when Sb is partially substituted in the parent compound. The high crystallinity for the Sb contained samples is the result of formation of fine particles. Using ImageJ program [58], the average particle size distributions for all samples are counted from their respective images. Figure 3.11 (b), (d), and (f) displayed the Gaussian fitted histogram data of the estimated particle size distributions. For the parent compound, the large particles are found in the micrometer (μm) order, while nanoparticles with the average sizes of 100~300 nm formed in Sb incorporated sample. The result shows the effect of Sb substitution in the good quality powder sample preparation. In fact, the particle size obtained in the present research are relatively smaller than previous reported [47]. In photocatalysis, nanoparticles with higher crystallinity are accountably considered as a good catalyst for high light conversion efficiency due to the quantum confinement effect.

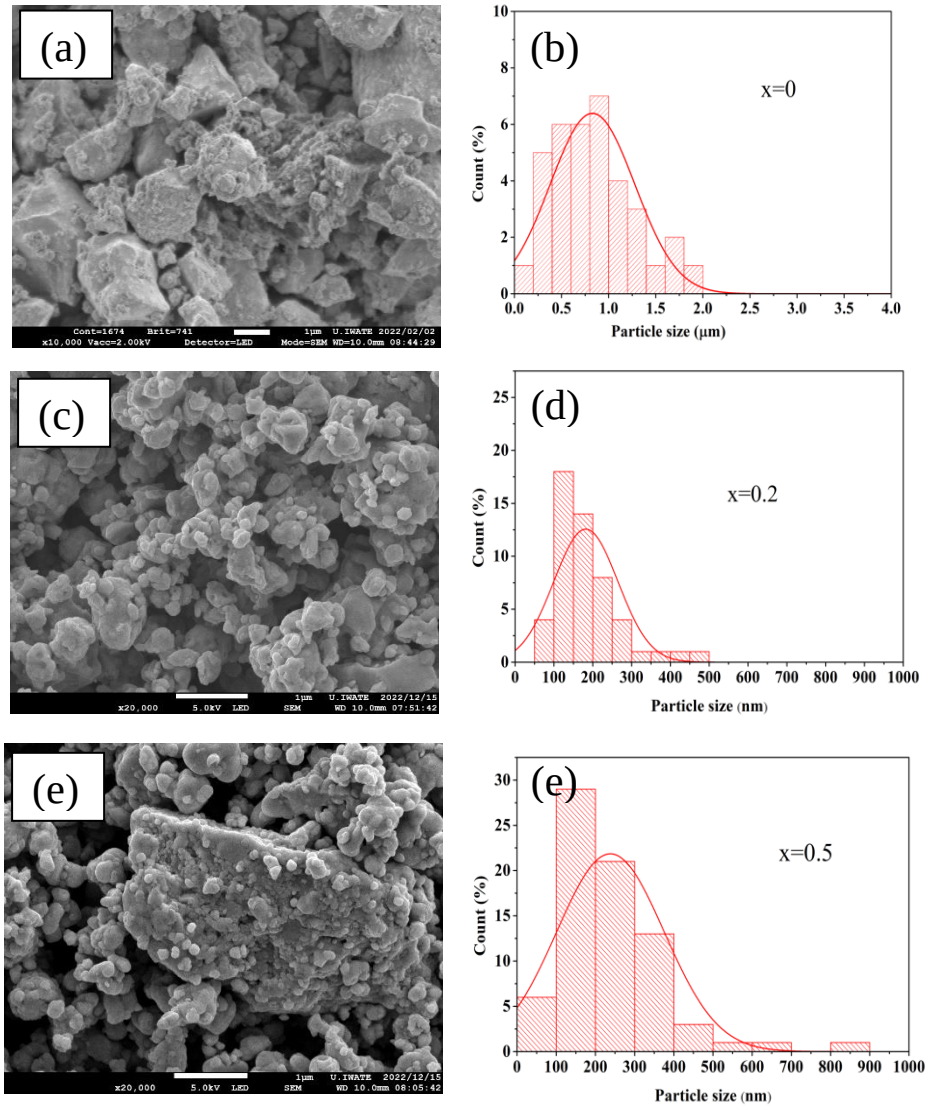

Figure 3.11: SEM images (in the left side) and and particle size distribution histogram (in the rigth side) of $Ba_2Bi^{3+}Bi^{5+}_{1-2x}Sb^{5+}_{2x}O_6$ for (a, b) x=0.0, (c, d) x=0.2, and (e, f) x=0.5 samples

3.6 Band gap estimation

A. $Ba_2TbBi_{(1-x)}Sb_xO_6$

In order to measure the optical properties of $Ba_2Tb(Bi_{1-x}Sb_x)O_6$ double perovskite band gap data were calculated with the help of Kubelka-Munk (KM) function [17, 20, 22]. At first, the data of diffuse reflectance from a spectroscopy (V550, JASCO Co.) were collected. Then it was transferred to the KM equation, and by drawing a tangent to the line, band gap was measured. In the KM formula of $(\alpha\varepsilon_p)^n \propto (\varepsilon_p - E_g)$, the power 'n' of absorption coefficient $(\alpha\varepsilon_p)$ used to determine the types of photo-electronic transition processes, like direct or indirect. Accordingly, the values n=2 and ½, respectively, are used for calculating direct and indirect band semiconductors. The term absorption coefficient $(\alpha_{KM}\varepsilon_p)^n$ in the Y-axis and photon energy (ε_p) were plotted in the X-axis. Finally, extrapolating a tangent intersecting the photon energies, consider the band gap energies. Figure 3.12 shows the band gap energies calculation curve for $Ba_2Tb(Bi_{1-x}Sb_x)O_6$ (x=0, 0.1, 0.5, and 0.6). For x=0 and 0.1, the data was plotted $(\alpha_{KM}\varepsilon_p)^{1/2} vs\ \varepsilon_p$, and respectively $(\alpha_{KM}\varepsilon_p)^2 vs\ \varepsilon_p$ for x=0.5 and 0.6 samples. The estimated band gap values are found to be 0.92 eV, 0.94 eV, 2.45 eV, and 2.59 eV for x = 0, 0.1, 0.5, and 0.6 samples, respectively. These values are also listed in Table 10. A phase transition related indirect to direct band transition at x=0.5 observed for $Ba_2Tb(Bi_{1-x}Sb_x)O_6$ compounds. Figure 3.12 (d) includes the band gap values of Pr-based compounds along with the $Ba_2Tb(Bi,Sb)O_6$ compounds in term of Sb values. The change in band gap energies with the variation of Sb(x) for $Ba_2Tb(Bi,Sb)O_6$ compound found similar characteristics with Pr-based compounds [22, 24]. In addition, the curve demonstrates band gap widening under Sb substitutions at Bi site, affecting the electronic structure of $Ba_2Tb(Bi,Sb)O_6$ samples. However, the large discrepancies at x=0.5 suspected for the twin phase

(monoclinic and cubic) present in Pr-based compounds have a reasonable effect on reducing the band gap size.

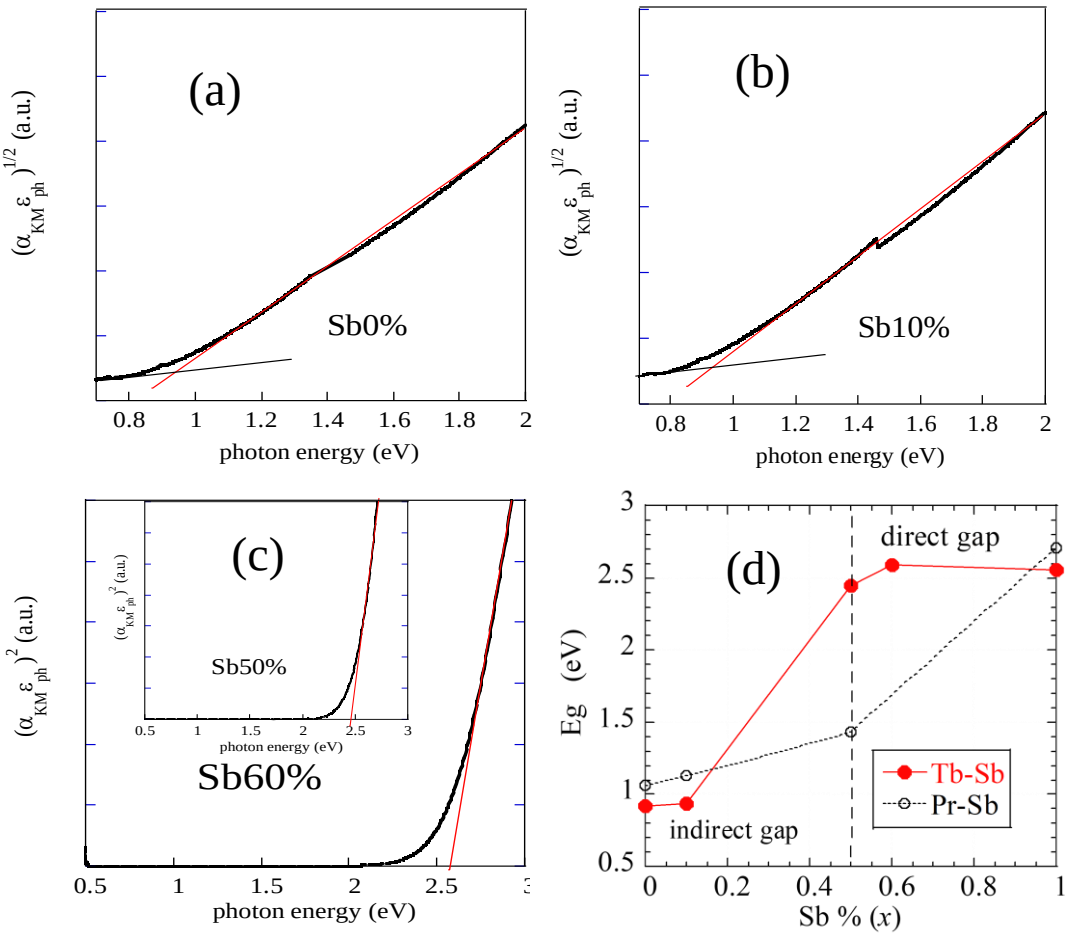

Figure 3.12: Band gap energy of $Ba_2Tb(Bi, Sb)O_6$ for (a) x=0, (b) x=0.1, (c) x=0.5 (inset) and 0.6, and (d) band gap values as a function of Sb

Table 10 Band gap energies of $Ba_2Tb(Bi, Sb)O_6$ for different x values

Sb(x)	0.0	0.1	0.5	0.6	1.0
E_g (eV)	0.92	0.94	2.45	2.59	2.56

Next, the reason for Sb substitution on band gap enlargement can be explored using first principle calculation. It is a theoretically designed density function theory (DFT) implemented in Quantum ESPRESSO [29, 30] package utilized to compute the electronic structure of $Ba_2Tb(Bi_{1-x}Sb_x)O_6$ compound. A clear picture of electronic state arrangement can be gleaned from the accurate crystallographic information. For this calculation, experimentally observed lattice parameters were imputed (as shown in Table 1and 2) [23, 51].

Figure 3.13 illustrates the energy band structure calculation for the parent and end member compounds. The estimated direct band gaps are found to be 1.90 eV and 3.77 eV for the parent and end member compounds, respectively. These values are quite higher than the experimental estimation. It can be attributed to the fact that the B-site partial disordering effect, responsible for the band gap narrowing, was not considered in the density of state calculation, which may reflect this result. In addition, the overestimation of band gap for the parent compound is probably related to the large band gap measurement in this study. For instance, the experimentally observed band gap of 0.89 eV of pristine $BaBiO_3$ was found to be 2.0 eV from theoretical prediction [59, 60]. However, the present estimation shows a good relationship with the previously reported theoretical values.

In previous study of density state calculation for $Ba_2Pr(Bi, Sb)O_6$ compound [22, 24], it was found that the upper part of the valence band (VB) associated with Bi^{3+}(6s) state, while lower part of the conduction band (CB) consists of Bi^{5+}(6s). Accordingly, in this present study for the parent Ba_2TbBiO_6 compound (as shown in Figure 3.13(a)), it is considered that Bi^{3+}(6s) and Bi^{5+}(6s) are the main contributors for the VB and CV.

However, substituting Sb in the end member compound Ba_2TbBiO_6 (seen in Figure 3.13(b)), the top of the CV shifted reasonably in the higher state, which leads to the band gap widening. Therefore, it is a matter of fact that Bi^{5+}(6s) states partially replaced by the Sb^{5+}(5s) electronic state.

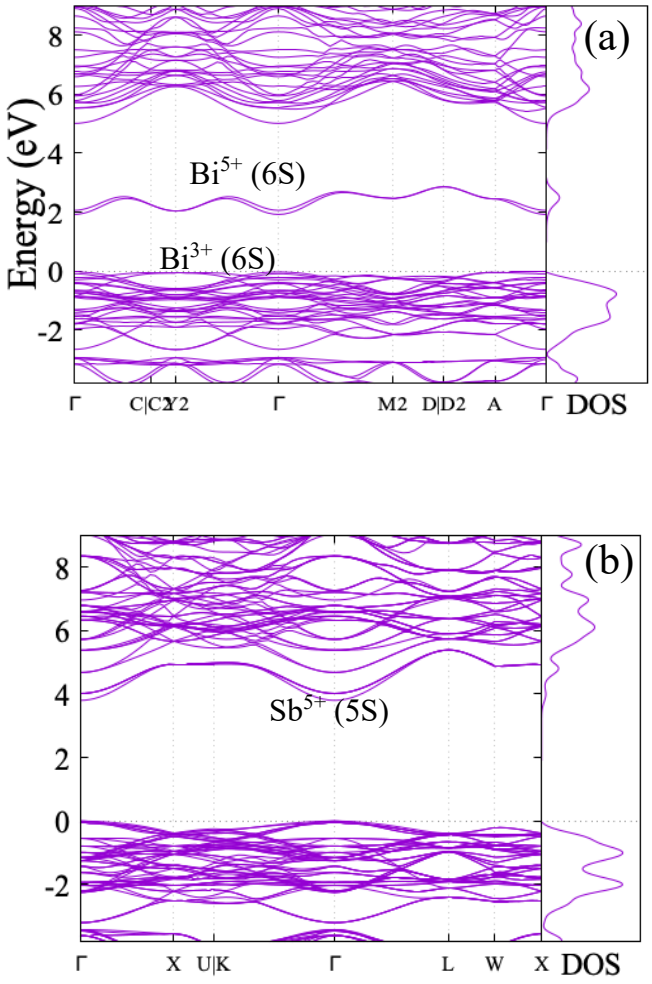

Figure 3.13: Energy band structures and total density of states near the Fermi levels for **(a)** monoclinic Ba_2TbBiO_6 and **(b)** cubic Ba_2TbSbO_6. Band gap values are 1.90 eV and 3.77 eV for the former and latter compounds, respectively

B. $\mathbf{Ba_2Bi^{3+}Bi^{5+}_{1-2x}Sb^{5+}_{2x}O_6}$

To elucidate the optical properties of $Ba_2Bi^{3+}Bi^{5+}_{1-2x}Sb^{5+}_{2x}O_6$samples band gap values are estimated using KubelKa-Munk function [17, 20, 22]. In this process, reflectance data were collected from a spectroscopy (V550, JASCO Co.) device are placed in the equation of KubelKa-Munk function and calculated the absorption coefficient (α_{KM}). Finally, in the extened form of α_{KM} with photon energy (ε_P), the band gap values are estimated from the extrapolation of $(\alpha_{KM}\varepsilon_P)^n vs\ \varepsilon_P$, following the equation $(\alpha_{KM}\varepsilon_P)^n \propto (\varepsilon_P - E_g)$. Here, it should be mentioned that the power term 'n' used to describe indirect and direct band gap phonon transition with the values ½ and 2, resepectively. Figure 3.14 represent the estimated direct and indirect band plots for $Ba_2Bi^{3+}Bi^{5+}_{1-2x}Sb^{5+}_{2x}O_6$ double perovskite semiconductor. In the whole range of x (from 0 to 0.5), both the direct and indirect band gap transitions are observed for the samples x=0, 0.1, and 0.2. Interestingly, switiching of band gaps to direct band phonon transition are seen from sample x=0.3 to the rest of the samples. It is expected that the plausible amount (30%) of Sb incorporation shifted this transition under unique electron correlation mechanism. In later section, the details mechanism will be discuused. The as estimated band gap values are listed in Table 11 and also plotted as a function of Sb concentration, displayed in Figure 3.14(d). However, band gap widdening as of Sb incorporation notiched for samples of $Ba_2Bi^{3+}Bi^{5+}_{1-2x}Sb^{5+}_{2x}O_6$ double perovskite oxide. This phenonmenon can be ascribed to the fact of smaller Sb^{5+}(0.6 Å) substitutions, considerably replaces the conduction band of BBO towards higher energy due to the relativistic effect with Bi^{5+}. According to the relativistic effect, the 5s electronic state energy of Sb is relatively in higher energy in compare to the Bi 6s electronic state [45]. Previous research on related compounds supported this findings and suggested that the conduction band of BBO associated with Bi^{5+} 6s electronic states suppressed via higher Sb^{5+} 5s electronic state rsulted in band enlargment [22, 59, 61].

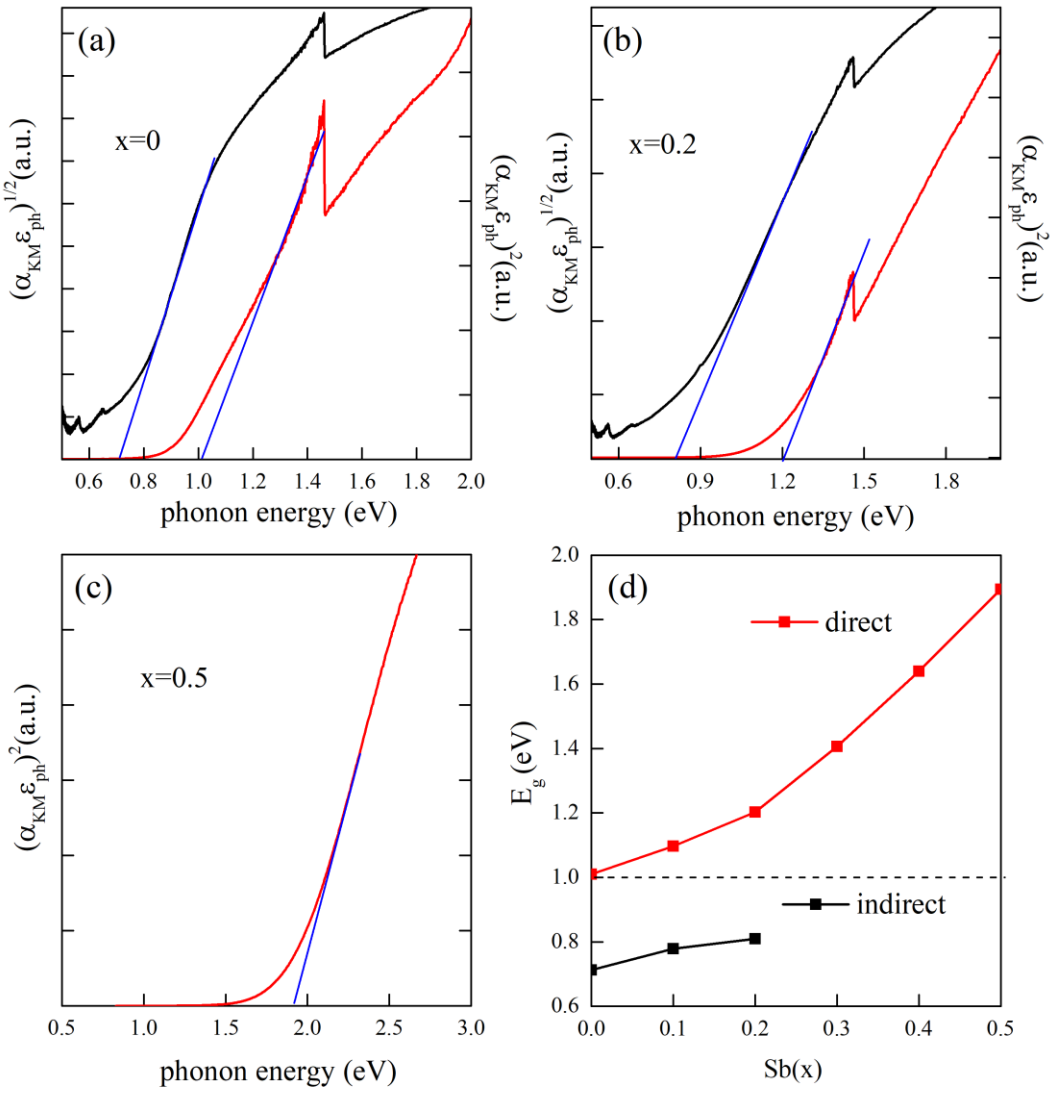

Figure 3.14: Kubelka-Munk function utilized band gap estimation of $Ba_2Bi^{3+}Bi^{5+}_{1-2x}Sb^{5+}_{2x}O_6$. The direct (red line) and indirect (black line) band gaps are calculated as $(\alpha_{KM}\varepsilon_P)^2 vs\ \varepsilon_P$ and $(\alpha_{KM}\varepsilon_P)^{1/2} vs\ \varepsilon_P$ for (a) x=0, (b) x=0.2, (c) x=0.5, and (d) band gap values as a function of Sb for $Ba_2Bi^{3+}Bi^{5+}_{1-2x}Sb^{5+}_{2x}O_6$(x=0, 0.1, 0.2, 0.3, 0.4, and 0.5) samples

Table 11 Estimated Band gap energies. Experimental band gap values are obtained from applying Kubelka-Munk function and Theoretical values are obtained from first principle calculation

Sb(x)	Band gap E_g in eV			
	Experimental		DFT calculation	
	Indirect	Direct	Indirect	Direct
0	0.7	1.0	0.88	2.01
0.1	0.8	1.1	-	-
0.2	0.8	1.2	1.05 (x=0.25)	2.20 (x=0.25)
0.3	-	1.1	-	-
0.4	-	1.6	-	-
0.5	-	1.9	1.73	2.92

In order to get a clear information regarding the Sb substitution effect on electronic structure of $Ba_2Bi^{3+}Bi^{5+}_{1-2x}Sb^{5+}_{2x}O_6$, first principle theory of density of state calculation is performed. Here, the whole computation is performed using Quantum ESPRESSO packae [33, 34], where Heyd–Scuseria–Ernzerhof hybrid functional (HSE06) [35,36] used for exchange correlation mechanism. The Seek-path [39] package was used to generate *k*-point path in the Brillouin zoneIn order to get the band structures and electronic density of states, the WANNIER90 program was used to build maximally localized Wannier functions [37], [38], [39], [40]]. In Figure 3.15, the calculated electronic structure of three main samples (x=0, 0.25, and 0.5) are displayed. To build the crystal structure of $Ba_2Bi^{3+}Bi^{5+}O_6$ [62], the obtained (experimentally) crystal phae *C*/2*m* and lattice parameters (as shown in Table 1) from Refined X-ray data are imputed. It is observed that the Bi^{5+} states in the conduction band and Bi^{3+} states with O^{2-} states in the valence band are predominantly contribute in the conduction of $Ba_2Bi^{3+}Bi^{5+}_{1-2x}Sb^{5+}_{2x}O_6$ samples. The seperation of these two distinct electronic states (Bi^{5+} and Bi^{3+}) are mainly responsible for band gap creation of

$Ba_2Bi^{3+}Bi^{5+}_{1-2x}Sb^{5+}_{2x}O_6$semiconductor. In addition, from the phase point analysis , the electron transition path is found between C (in the valence band maximum) and L_2 (in the conduction band minimum). Accordingly, the indirect (E_g^i) and direct (E_g^d) band gaps for the parent BBO compound (as seen in Figure 3.15(a)) is estimated to be 0.88 eV and 2.01 eV, correspondingly. In compare to the previously reported result [59, 63], these values are good agreement to support the present research. In the next compound, 25% of Bi^{5+} is partially replaced with Sb^{5+} to vissualize the Sb substitution effect on BBO. The calculated electronic structure are delinated in Figure 3.15(b). It is clearly vissible in Figure 3.15(b) that the lower part of the conduction slightly shifted to higher energy and resulted in a large band gap. The estimated band gap values are $E_g^i = 1.05\ eV$ and E_g^i=2.23 eV, respectively. Furthermore, increasing Sb concentration to the maximum (50%) for the complete reduction of Bi^{5+} at the end member compound (x=0.5), the indirect and direct band energies are calculated and shown in Figure 3.15(c). The values are found to be further increased at $E_g^i = 1.73\ eV$ and E_g^i=2.92 eV, respectively.

The above calculation suggests Sb incorporation perturb the bottom part of the conduction band of $Ba_2Bi^{3+}Bi^{5+}_{1-2x}Sb^{5+}_{2x}O_6$samples. However, the present calculation shows good approximation with the experimentally estimated band gap values. The discrepecy in the indirect band transition compare to experimental result for the end member $Ba_2Bi^{3+}Sb^{5+}O_6$ compound is suspected to the disordering phenomenon reflected to this result. Further correction in crystal structure and lattice parameters adjustment between experimental and theoretical results may lead to the proper understanding.

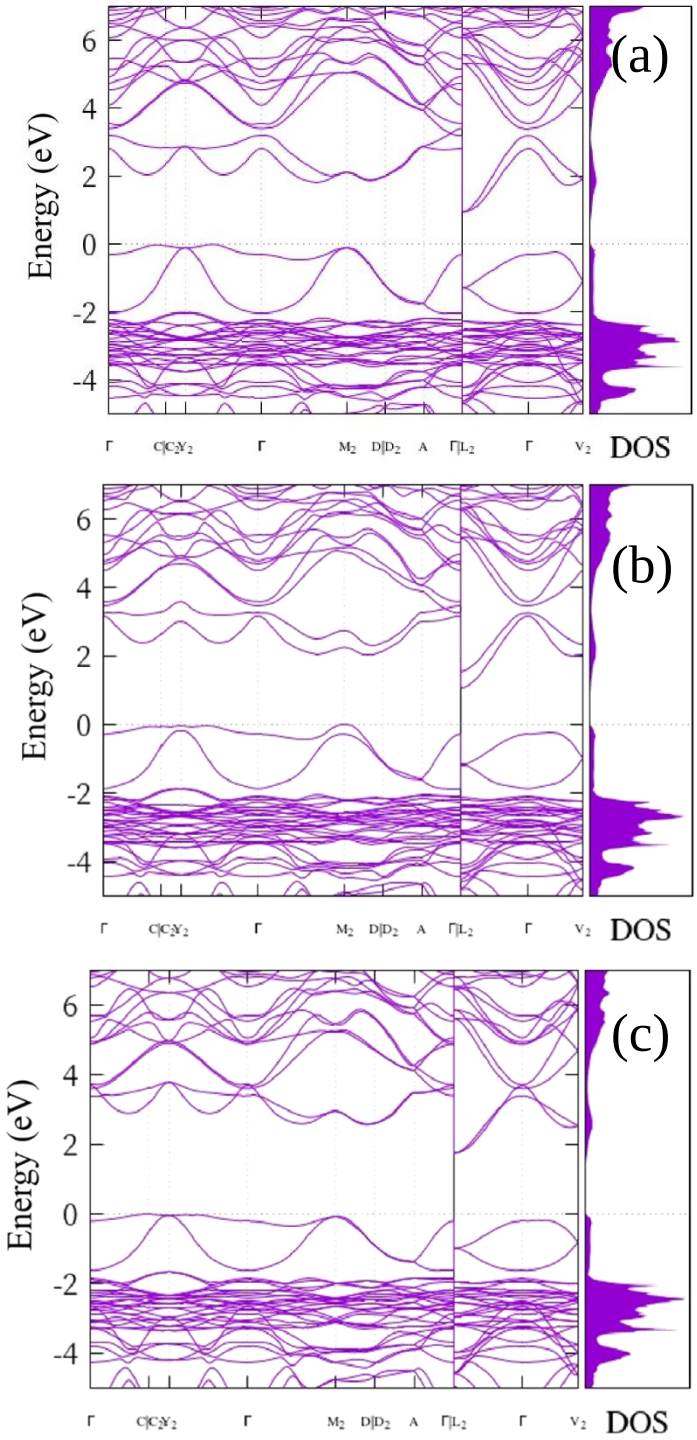

Figure 3.15: Density of State calculated energy band diagram of $Ba_2Bi^{3+}Bi^{5+}_{1-2x}Sb^{5+}_{2x}O_6$for (a) $Ba_2Bi^{3+}Bi^{5+}O_6$ (x=0), (b) $Ba_2Bi^{3+}Bi^{5+}_{0.5}Sb^{5+}_{0.5}O_6$, and (c)) $Ba_2Bi^{3+}Sb^{5+}O_6$. The Fermi level is 0 eV

3.7 Photocatalytic Properties

MB Degradation

A. $Ba_2TbBi_{(1-x)}Sb_xO_6$

The photocatalytic activities of $Ba_2Tb(Bi,Sb)O_6$ photocatalyst were examined through MB degradation performance. In this experiment, a predetermined concentration of MB solution with $Ba_2Tb(Bi,Sb)O_6$ photocatalyst was placed in a dark condition under continuous stirring for 30 minutes to obtain an absorption desorption equilibrium state. After that, the solution was transferred to the visible light illumination center, and at every 30-minute interval, the degradation was measured. MB self-degradation performance was checked in the absence of a catalyst by exposing it to visible light. The degradation was assessed in terms of MB concentration from the absorption peak intensity detected around λ = 665 nm using a UV visible spectrometer. It should be noted that the peak at λ = 665 nm is responsible for the MB concentration. Figure 3.16(a) depicts the absorption spectra of $Ba_2Tb(Bi,Sb)O_6$ (x = 0.6) sample for every 30 minute interval. The beginning data at the o minute count was taken into consideration as the initial MB concentration, represented by C(0), and the t-time interval concentration was denoted by C(t). Finally, calculated the MB degradation using the formula [25]

$$D = \frac{C(0)-C(t)}{C(0)} \times 100 \qquad \text{Equ. (3)}$$

Where D stands for degradation percentage of MB.

The degradation percentages for all samples are calculated and plotted as a function of irradiation time, which are delineated in Figure 3.9 (c).

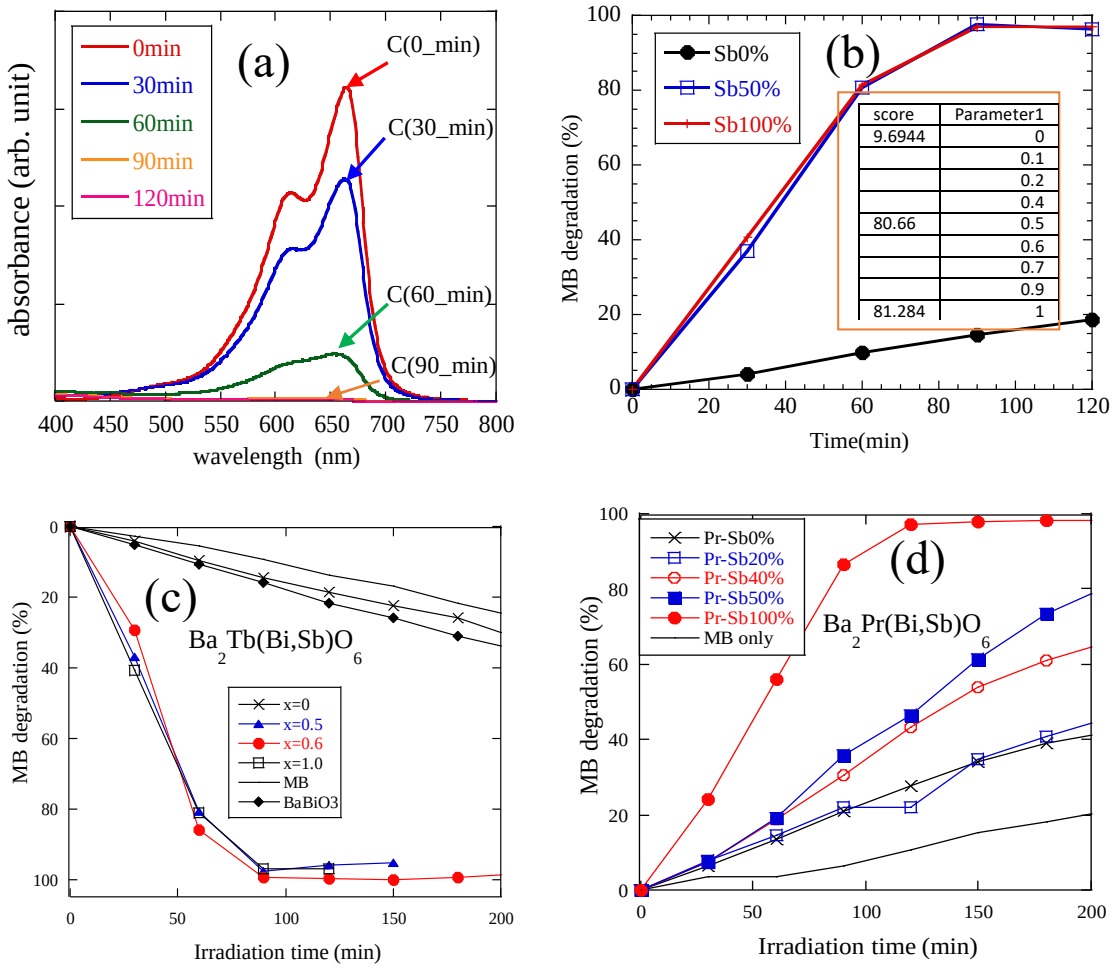

Figure 3.16: Photocatalytic MB degradation (a) absorption spectra, (b) Machine learning prediction, (c) $Ba_2Tb(Bi,Sb)O_6$, and (d) $Ba_2Pr(Bi,Sb)O_6$ Photocatalyst.

The self-degradation of MB is found to be very less, implies MB is not photodegradable. However, the degradation rates for $Ba_2Tb(Bi,Sb)O_6$ catalysts can be categorized into two types on basis of Sb substitution (as shown in Figure 3.16 (c)). In the first type without Sb concentration, the photocatalytic performance is found to be low. The result shows similar degradation of pristine $BaBiO_3$ sample. In contrast, the second type of catalyst

with larger Sb ($0.5 \leq x \leq 1.0$) values exhibits much greater degradation rates, while x=0.6 sample reported the highest degradation. It is expected that the photocatalytic active sites of the powder samples largely promoted under Sb substitution on Bi-site and optimized against the number of MB molecules around x=0.6. Furthermore, the high-quality fine particle formation in the citrate technique, as observed from SEM images, reflects this result. Former research on the ability to produce good quality particles by citrate method for $Ba_2Pr(Bi,Sb)O_6$ sample also supported this finding [22]. Further explanation on the reason for higher performances in the Sb-substituted samples will be discussed in the next section.

However, there are some comments on selecting the Tb-based x=0.6 sample. In the current research history, machine learning program achieved a milestone in efficiently predicting new materials with the desired properties [64]. This is an experimental data driven designed program, where few experimental data are prerequisite to perform the process. In this process, less experimental data is needed to predict the expected compound with suitable combinations. For instance, in case of $Ba_2Tb(Bi_{1-x}Sb_x)O_6$ compound, three experimentally observed MB degradation data sets (Sb content, MB degradation) respectively for (Sb)x=0, 0.5, and 1.0 were imputed to the machine learning program (Common Bayesian Optimization library, COMBO.exe [65]). Subsequently, x=0.6 was recommended as a next candidate for better MB degradation performances. Interestingly, this prediction was matched while performing the experiments. Although, there is little difference in MB degradation rate percentage, the composition was perfectly matched. The whole operation procedure is clearly represented in Figure 3.16 (b). Furthermore, to make comparison with the previous study of Pr-based catalyst, photocatalytic MB degradation performances of $Ba_2Pr(Bi,Sb)O_6$ are also plotted, which is displayed in Figure 3.16(d). As observed in Figures 3.9 (c) & (d), Sb substitution in Tb-based compound MB degradation rates enhanced significantly, while only the end

member sample Ba_2PrSbO_6 exhibited better catalytic activities. It should be noted that the MB degradation rates increase with photocatalytic reductive reactions, and it is considered that Sb-substitution promotes more reduction reactions in $Ba_2(Pr,Tb)(Bi,Sb)O_6$ photocatalyst. However, the lower band gap factors may affect the reductive reaction rates of $Ba_2(Pr,Tb)(Bi,Sb)O_6$, resulting in poor catalytic performances. The higher band gap 2.59 eV of x=0.6 compound in comparison to x=0.5 (2.45 eV), and 1.0 (2.56 eV) listed in Table 12 showed clear evidence of the highest photocatalytic performance. Moreover, the previous research on relevant perovskite compounds, including manganite, titanate, ferrite, and niobium perovskites, has also been accounted for in this research, and a comprehensive analysis has been made.

Table 12 Visible light illuminated photocatalytic MB and IPA decomposition of $Ba_2(Tb,Pr)(Bi, Sb)O_6$

For $Ba_2Tb(Bi, Sb)O_6$

Sb(x)	0.0	0.1	0.5	0.6	1.0	$BaBiO_3$
MB (%)	32	-	97	100	96	36
CO_2 (ppm/g)	221	204	32	-	-	-
For $Ba_2Pr(Bi, Sb)O_6$						
MB (%)	42	32	80	-	98	
CO_2 (ppm/g)	221	204	32	-	-	

For the pristine $BaBiO_3$ perovskite, the MB degradation rates were observed in the same manner as for the $Ba_2(Pr,Tb)(Bi,Sb)O_6$ photocatalyst, and the data are enlisted in Figure 3.16 (c). As shown in Figure 3.16 (c), the degradation rates are found to be similar to the parent $Ba_2(Pr,Tb)BiO_6$. In contrast, Tang et al. prepared the same $BaBiO_3$ perovskite, showed high photocatalytic activities [17]. The higher performance in the later sample can be ascribed to the fact that the band gap magnitude 2.05 eV which is relatively higher than estimated 0.83 eV. In addition, the way of sample preparation is also an important

factor that contributed to the photo-induced reaction active sites on the powder catalyst surface. However, considering with other compounds assigned in Table 13, present $Ba_2Tb(Bi,Sb)O_6$ compounds exhibits better photocatalytic performances.

Table 13 Photocatalytic MB degradation performances of different perovskite catalyst

Catalyst	Initial MB (mg/L)	Mass (mg)	Time (min)	Degradation rate (%)
$Ba_2Tb(Bi_{1-x}Sb_x)O_6$ (x=0.6)	10	200	90	100
$Ba_2Pr(Bi_{1-x}Sb_x)O_6$ (x=1.0) [22]	10	200	90	100
$BaBiO_3$ [17]	15.3	300	60	100
$Nd_{0:7}Ca_{0:3}MnO_3$ [45]	10	40	180	96
Fe-doped $CaTiO_3$ [46]	10	100	180	100
Y-doped $BiFeO_3$ [47]	50	100	120	97.6
$NaNbO_3$ [48]	10	160	180	99.3

B. $\mathbf{Ba_2Bi^{3+}Bi^{5+}_{1-2x}Sb^{5+}_{2x}O_6}$

To investigate the catalytic activities, MB degradation performance of the rare-earth free $Ba_2Bi^{3+}Bi^{5+}_{1-2x}Sb^{5+}_{2x}O_6$ (x=0, 0.1, 0.2, 0.3, 0.4, and 0.5) powder samples has been examined under visible light illumination. Here, the degrataion rate is calculated from the respective concentration of MB present in a particular catalyst suspended MB solution as a function of irradiation time. A simple mathematical formula used to calculate this rate percentage as $(C(0) - C(t))/C(0) \times 100\%$, where $C(0)$ and $C(t)$ represent the initial and final MB concentration for different times, respectively. Figure 3.17 exhibits the Sb dependent MB degradation properties of $Ba_2Bi^{3+}Bi^{5+}_{1-2x}Sb^{5+}_{2x}O_6$(x=0, 0.1, 0.2, 0.3, 0.4, and 0.5) samples as a function of time. It is worth mentioning that the concentrations

C(0) and $C(t)$ are measured in term of absorption peak intensity using a UV-visible spectroscopy. The presence of MB can be identified by visualizing a peak at 665 nm in the absorption curve. For instance, in Figure 3.17(a), the decreasing of the absorption peaks at wavelength 665 nm in case of $Ba_2Bi^{3+}Bi^{5+}_{0.6}Sb^{5+}_{0.4}O_6$ sample is responsible for MB degradation. Initially, the self-degradation of MB has been carried out and the rate is found to be quite low suggested MB itself not degradable. In fact, the parent compound BBO also exhibit poor catalytic activities and yielded in equivalent to the MB itself. In compare to the previous research of BBO [17, 26], it is suspected that sample preparation and other factors may reflected to this present result. Next, for the Sb substituted samples, the degradation of MB into colorless LMB is found to be remarkably enhanced, while maximum degradation (50%) observed for 20% Sb incorporated sample. The degradation results are also displayed in Table 14. It is expected that the effect of Sb substitution in BBO, promoted more active sites on the surface of powder sample resulted in a good catalytic performance. In addition, the quantum confinement effect due to nanoparticles formation in the Sb content samples made them excellent for unique photoconversion efficiency.

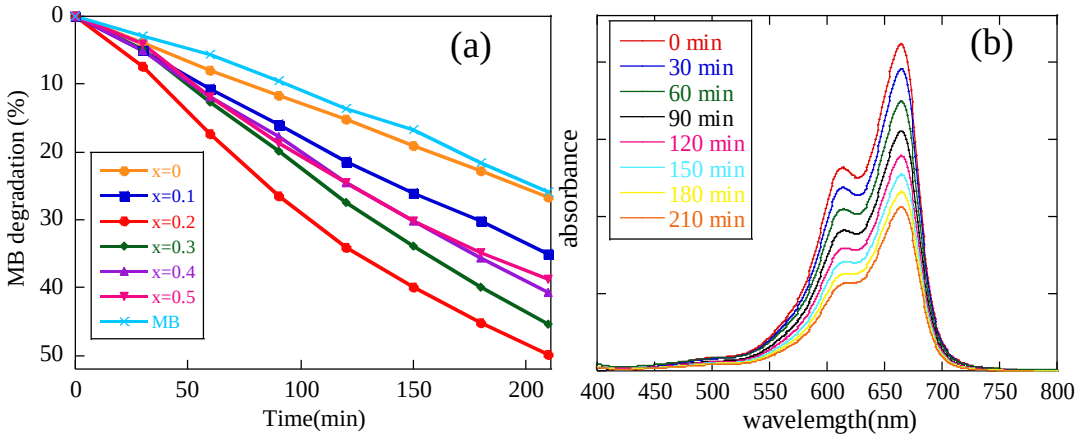

Figure 3.17: Visible light irradiated photocatalytic properties of $Ba_2Bi^{3+}Bi^{5+}_{1-2x}Sb^{5+}_{2x}O_6$(x=0, 0.1, 0.2, 0.3, 0.4, and 0.5). (a) MB degradation for different Sb loading and (b) Absorption spectra as a function time

Former investigation on Sb dependent enhanced MB degradation performance is good evidence to support this result [22, 61]. However, for the particular sample (x=0.2), the highest degradation rate is considered to be the result of optimized photo active sites instead of the number of MB dye molecules effectively converted into hydroxyl and superoxide radicals [26, 66]. Furthermore, the quantum confinement effect more sensitive for nano size particles [67] may reflected to this present research. These above factors are accounted for the improvement of present $Ba_2Bi^{3+}Bi^{5+}_{1-2x}Sb^{5+}_{2x}O_6$ samples. The detail catalytic reaction mechanism will be discussed in the next section.

Table 14 Photocatalytic MB and IPA decomposed CO_2 evaluation for $Ba_2Bi^{3+}Bi^{5+}_{1-2x}Sb^{5+}_{2x}O_6$. Irradiation time = 210 minutes

Sb x	MB degradation rate (%)	CO_2 evaluation (ppm/g)
0.0	27	658
0.1	35	-
0.2	50	209
0.3	45	-
0.4	41	-
0.5	39	288

Furthermore, the current findings compared with the previously reported rare-earth based double perovskite and other relevant compounds, as shown in Table 15. Accordingly, the MB degradation for rare-earth based $Ba_2R^{3+}Bi^{5+}O_6$ (R=La, Ce, Nd, Sm, Eu, Gd, and Dy) compounds reported by Hatakeyama research group [20] is listed in Table 15 (displayed only the highest performance). In their investigation, they noticed maximum degradation rate approximately 73.4% and 73.9% in case of $Ba_2Ce^{3+}Bi^{5+}O_6$, and $Ba_2Sm^{3+}Bi^{5+}O_6$ compounds, respectively, among seven compounds. However, comparing with the present research, they used very low amount of MB dyes (1/3 times smaller), high amount of catalyst (about 2.5% times higher), and long light exposing duration (480 minutes>

210 minutes). Considering these factors, present research of 50% degradation result for $Ba_2Bi^{3+}Bi^{5+}_{1-2x}Sb^{5+}_{2x}O_6 (x = 0.2)$ is obviously exhibits better performance. In fact, the performance is even better than the previously synthesized rare-earth compounds Ba_2(Pr, Tb)$Bi^{5+}O_6$ [61]. Furthermore, the data has been analyzed with the catalytic performance of pristine BBO compounds [17, 26]. As mentioned above, the good sample preparation technique and other factors might be reflected in the former research. However, present investigation shows comparatively better photocatalytic ability than rare-earth based compounds under Sb substitution.

Table 15 Photocatalytic MB degradation performance analysis with rare-earth based double perovskite and other relevant compounds

Catalyst type	Initial MB concentration (mg/L)	Catalyst amount (ppm/g)	Light duration (min)	Degradation rate (%)
$Ba_2Bi^{3+}Bi^{5+}_{1-2x}Sb^{5+}_{2x}O_6$ $(x = 0.2)$	10	200	210	50
$BaBiO_3$[17]	15.3	300	60	100
$BaBiO_3$[26]	15	100	240	83
Ba_2(Pr, Tb)$Bi^{5+}O_6$[61]	10	200	90	~42
Ba_2RBiO_6(R=Ce) [20]	3.20	500	480	73.9

IPA Decomposition

A. $Ba_2TbBi_{(1-x)}Sb_xO_6$

In respect to the MB degradation, photocatalytic gaseous 2-propanol (IPA) decomposition performances were conducted under visible light illumination to further support the catalytic properties of Ba_2(Pr,Tb)(Bi,Sb)O_6 double perovskite. In this procedure, a glass reactor containing powder catalyst was exposed to visible light, and

after a predetermined interval, the amount of CO_2 evolution was measured using a gas chromatograph.

Figure 3.18 illustrates the photocatalytic IPA decomposition in terms of CO_2 evolution performances of $Ba_2Tb(Bi,Sb)O_6$ compounds as a function of irradiation time. It should be noted that the CO_2 evolution was normalized by the BET surface area of the samples.

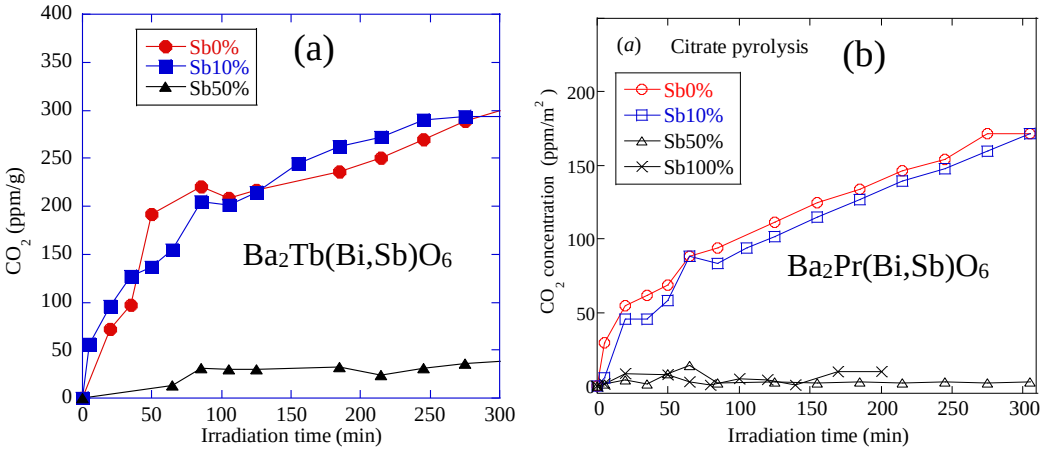

Figure 3.18: Visible light driven photocatalytic CO_2 evolution performances of (a) $Ba_2Tb(Bi,Sb)O_6$ and (b) $Ba_2Pr(Bi,Sb)O_6$ [22] as a function of irradiation time

As seen in Figure 3.18, the rate of CO_2 evolution for the first 20 minutes is very faster than subsequent rates and decreases as irradiation time progresses, eventually reaching a steady state. The problem is associated with the absorption process of the generated CO_2 gaseous on the surface of the sample [22]. As described in the experimental section, the photo-induced IPA to CO_2 conversion reaction took place on the surface of the powder catalyst, where the effective electrons and holes are generated. After the immediate reactions, the slower movement of CO_2 gaseous creates a contacting layer that prevents

the next IPA molecules from reaching the surface of the sample, resulting in a decrease in CO_2 concentration. In case of Tb-based compound, the significant amount of CO_2 evolution was obtained for x=0 and 0.1 sample. Nevertheless, at x=0.5 and higher Sb content compounds, no notable contribution to the IPA decomposition was detected. Compounds $Ba_2Pr(Bi,Sb)O_6$ also exhibited the same features of IPA breakdown as shown in Figure 3.18 (b).

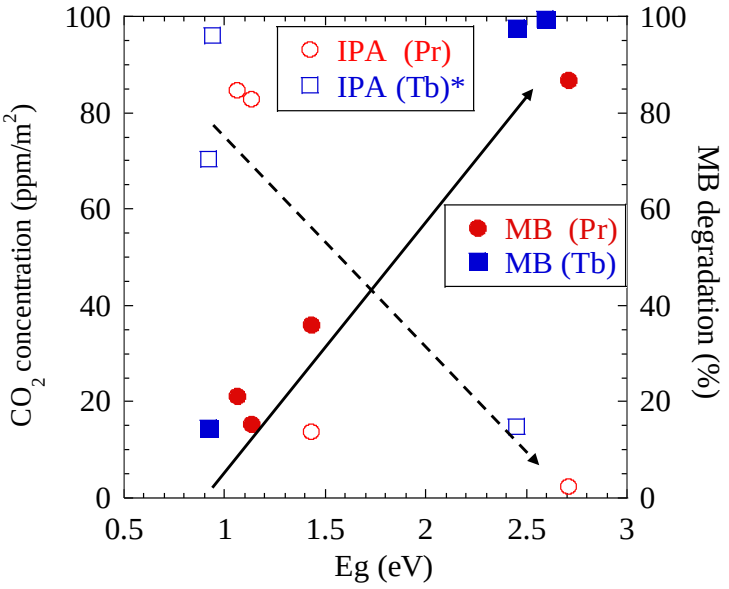

Figure 3.19: Photocatalytic activity as a function of band gap energy for $Ba_2(Pr,Tb)(Bi,Sb)O_6$

Large band gaps are expected to have a reasonable impact on the CO_2 conversion performances. The oxidation reactions that carry out the photocatalytic IPA decomposition generally use electron and hole counts as a driving force to enhance the catalytic activities. As a result, smaller band gap materials are sufficient enough to perform better catalytic activities upon supplying large number of charge carriers to promote the oxidation reaction. Consequently, it can be stated that the increase in band

energy caused by Sb substitution simultaneously hindered IPA decomposition efficiency. For clarity, the IPA and MB decomposition results are plotted in Figure 3.19 against Sb values as well as band gap energies. Figure 3.19 demonstrates a direct correlation between MB degradation and IPA decomposition, with MB exhibiting a rising trend with band gap values. In contrast, IPA results show the exact opposite of the MB observation.

B. $\mathbf{Ba_2Bi^{3+}Bi^{5+}_{1-2x}Sb^{5+}_{2x}O_6}$

To support the catalytic actitvities, gases 2-propanol (IPA) decomposition of $Ba_2Bi^{3+}Bi^{5+}_{1-2x}Sb^{5+}_{2x}O_6$(x=0, 0.1, 0.2, 0.3, 0.4, and 0.5) samples are performed under visible light irradiation. In this experiment, photocatalytic IPA decomposition of three main samples (x=0, 0.2, and 0.5) has been examined. The obtained results are displayed in Figure 3.20, also listed in Table 14. It is mentioning that the CO_2 evaluation is normalized by samples amount. As can be seen from Figure 3.20, the faster decomposition rate in the initial 20 minutes readily goes down to saturation level with illumination time. This phenomenon is attributed to the adsorption of resulted CO_2 adsorption on the surface of the powder sample, pretend further IPA oxidation.

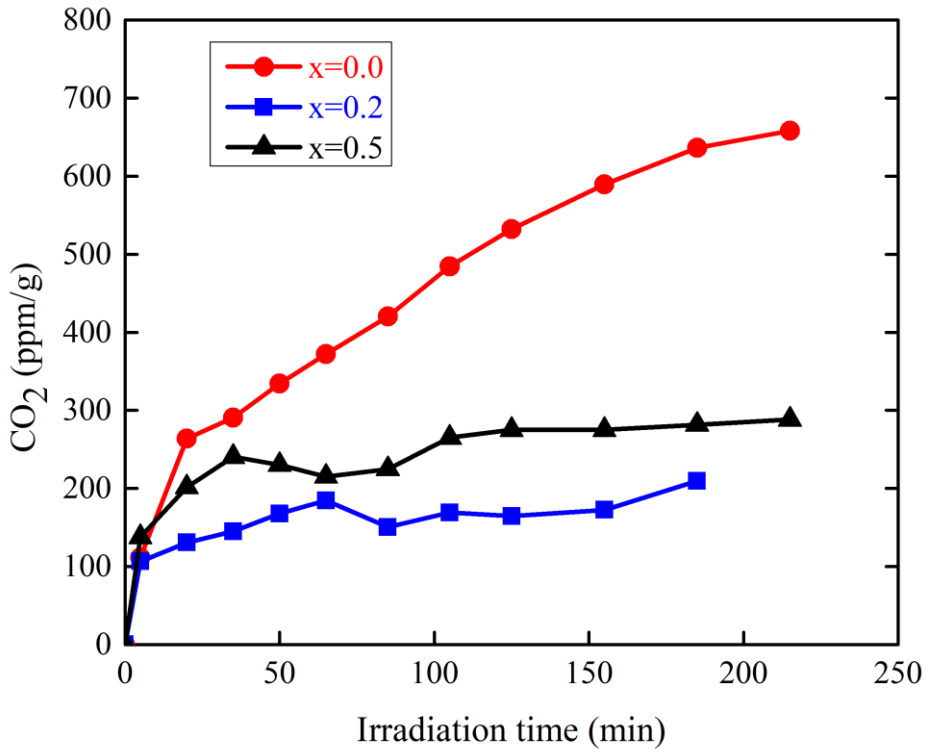

Figure 3.20: Photocatalytic IPA decomposition measurement in terms of amount of CO2 evolution as a function of time for $Ba_2Bi^{3+}Bi^{5+}_{1-2x}Sb^{5+}_{2x}O_6$sample

However, the highest yield in CO_2 (658 ppm/g) i.e., good IPA conversion efficiency noticed for x=0 sample. In case of Sb substituted samples, this performance is found to be quite low. It is expected that nanoparticles with relatively higher band gap in the Sb substituted samples strongly affect the IPA oxidation reaction resulted in a poor performance.

3.8 Photocatalytic Mechanism

A. $Ba_2TbBi_{(1-x)}Sb_xO_6$

Band energy positions of a catalyst in the normal hydrogen electrode (NHE) are indispensable for comprehending the photocatalytic mechanism. The NHE provides information regarding the ability to facilitate photocatalytic oxidation or reduction reactions in terms of the band edge potentials of VB and CB. It is well known that a catalyst must possess a minimum potential energy in order to execute any catalytic reaction, whether oxidation or reduction. According to the NHE scale, the VB potential must be at least 1.23 eV or greater for oxidation, and the CB potential must be at least 0 eV or greater in the negative. To illustrate the photocatalytic ability of Ba_2(Pr,Tb)(Bi,Sb)O_6 compounds, a schematic diagram of their band edge positions is represented in Figure 3.21. The band edge positions E_{CB}(for CB), and E_{VB}(for VB) of Ba_2(Pr,Tb)(Bi,Sb)O_6 were calculated using the following formula [15, 16]:

$$E_{CB} = \chi - E^e - 0.5E_g \quad (3)$$

$$\text{And, } E_{VB} = E_{CB} + E_g \quad (4)$$

Where χ, E^e, and E_g represents the electronegativity, free electron energy, and band gap value of the semiconductor, respectively. In the hydrogen scale, the free electron energy is estimated to be around 4.5 eV. However, the term "χ" is a complex quantity that depends on the chemical formula and the atoms that form the compound. It can be computed using the geometric mean of the electronegativities of the individual atoms in the compound. For the present $Ba_2Tb(Bi_{1-x}Sb_x)O_6$ samples, the χ was calculated as a function of Sb(x) content using the formula [17, 72]

$$\chi = [\chi^2(Ba)\chi(Tb)\chi^{1-x}(Bi)\chi^x(Sb)\chi^6(O)]^{1/10} \quad (5)$$

Where the individual electronegativities of each atom in the right part of equation (5) were calculated from their arithmetic average of electron affinity and first ionization energy [73].

Table 16 Photocatalytic properties of $Ba_2(Tb,Pr)(Bi,Sb)O_6$ as function of band edge potential (E_{CB}, E_{VB}) in normal hydrogen electrode potential scale

Catalyst	Sb(x)	Band gap (eV)	Band edge potential (eV)		MB (%)	CO_2 (ppm/g)
			E_{CB}	E_{VB}		
$Ba_2Tb(Bi,Sb)O_6$	0.0	0.92	0.337	1.257	32	221
	0.1	0.94	0.336	1.276	-	204
	0.5	2.45	-0.384	2.066	97	32
	0.6	2.59	-0.445	2.145	100	-
	1.0	2.56	-0.395	2.165	96	-
$Ba_2Pr(Bi,Sb)O_6$	0.0	1.06	0.268	1.328	42	
	0.5	1.43	0.127	1.557	80	
	1.0	2.71	-0.469	2.241	98	
$BaBiO_3$		0.92	0.521	1.341	36	-

For instance, the Ba atom has an electron affinity of 0.144582 eV and a first ionization energy of 5.2117 eV. Therefore, Ba's electronegativity, $\chi(Ba)$, ought to be 2.678141 eV. The electronegativities of other atoms were computed in a similar way, leading to the final calculation of χ. By putting these values in Equ. (3) and (4), estimated the CB and VB edge positions and listed them in Table 16. These data are also represented in the NHE, as displayed in Figure 4.0It is evident that the VB edge potentials of the compounds with lower Sb values (x=0 and0.1) are 1.26 and 1.28 eV, respectively, which are comparatively sufficient to support the oxidation reaction. However, their CB edge

potential 0.34 eV (x=0 and 0.1) is not enough for reduction mechanism. Next, for the higher Sb (x=0.5, 0.6, and 1.0) values compound, the estimated CB edge potentials -0.38 eV, -0.45 eV, and -0.40 eV show more negative to the potential and exhibit higher effective reduction abilities. Comparing Pr-based compounds, it is found that only the end member candidate Ba_2PrSbO_6 has the capacity to support an efficient reduction process, according to the CB edge potential estimates of 0.23 eV and -0.51 eV for the parent and end member compounds, respectively. It is noted that the higher CB negative potential estimated for $Ba_2TbBi_{0.4}Sb_{0.6}O_6$ and Ba_2PrSbO_6 samples remarkably exhibited better reduction kinetics. Therefore, it is inevitable from the above analysis that compounds with lower Sb values and smaller band gap energies are well-suited for photocatalytic oxidation reactions related to IPA decomposition.

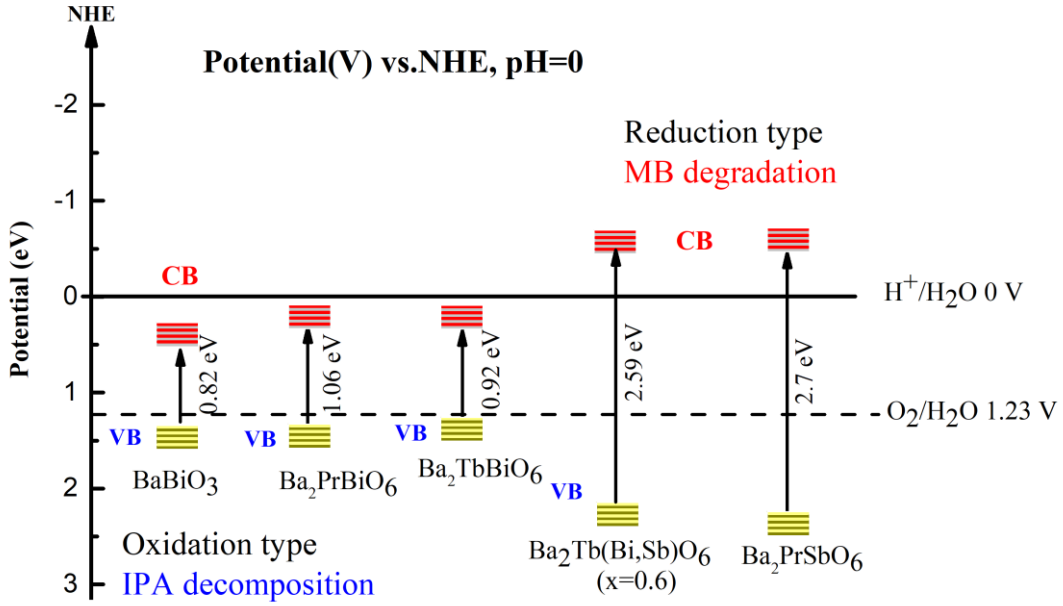

Figure 3.21: Band edge potential facilitated photo-induced charge separation and their relative catalytic oxidation and reduction dependent IPA and MB decomposition

Conversely, photocatalytic MB reduction reactions are observed in the compound that has a high Sb substitution and comparatively higher band gap energies. The results of the photocatalytic MB and IPA decomposition experiments are in good agreement with these findings.

B. $\mathbf{Ba_2Bi^{3+}Bi^{5+}_{1-2x}Sb^{5+}_{2x}O_6}$

Flat band potential in the normal hydrogen electrode potential is used to explain the photocatalytic mechanism of $Ba_2Bi^{3+}Bi^{5+}_{1-2x}Sb^{5+}_{2x}O_6$ in terms of photocatalytic oxidation and reduction reactions, respectively. This method considers the actual chemical electronegativities of the constituent atoms as a whole in the compound and can accurately predict the electrochemical potential for the semiconductor materials. Figure 10 illustrates the VB and CB edge potentials of $Ba_2Bi^{3+}Bi^{5+}_{1-2x}Sb^{5+}_{2x}O_6 (x = 0 \text{ and } 0.5)$ and different rare-based double perovskite compounds. According to NHE, the degree of reduction reactions responsible for MB decomposition is a function to which CB edge potential is more negative. In contrast, photocatalytic oxidation of IPA is completely related to the number of holes created in the VB. The calculation of flat band potentials in Figure 3.22 clearly stated that the CB edge potential for Sb substituted sample (x=0.5) located to facilitate photocatalytic reduction reaction resulted in good MB degradation performance. On the other hand, the VB edge potential for parent (x=0) and rare-earth based compounds promoted more holes in the VB due to smaller band, resulted in good IPA decomposition performance.

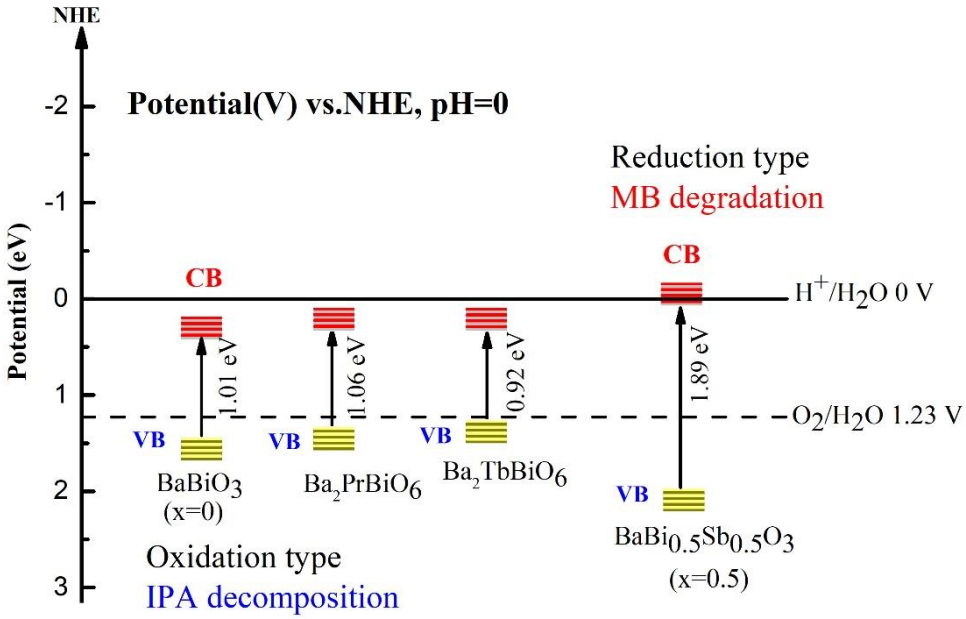

Figure 3.22: Flat Band edge potential calculation for $Ba_2Bi^{3+}Bi^{5+}_{1-2x}Sb^{5+}_{2x}O_6 (x = 0 \text{ and } 0.5)$, Ba_2PrBiO_6, and Ba_2TbBiO_6

Chapter 4

Conclusion

In this present thesis, two approaches, one of rare-earth-based $Ba_2Tb(Bi_{1-x}Sb_x)O_6$ double perovskite and the other of rare-earth-free $Ba_2Bi^{3+}Bi^{5+}_{1-2x}Sb^{5+}_{2x}O_6$ double perovskite oxide, were considered for investigation. The effect of Sb substitution on the structural, magnetic, band gap energies, and photocatalytic properties of these two semiconductors was clearly explained. The key parameters that lead to the visible light-driven enhancement of photocatalytic performance and their mechanisms were gently addressed in this research. Accordingly, crystal structural stability, improved surface morphology, and energy band potential are considered for the enhancement of the catalytic activities of the investigated catalysts. The band gap widening effect due to Sb substitution observed in the experimental estimation of Kubelka-Munk function is explained through DFT calculations. It was found that the upper part of the CB, consisting of Bi^{5+} (6s), was partially replaced by the higher Sb^{5+} (5s) state, resulting in a larger gap between VB and CV. The photocatalytic properties of rare-earth-based samples $Ba_2Tb(Bi_{1-x}Sb_x)O_6$ are found to be literally higher (100%) than those of the existing relevant compounds and rare-earth free $Ba_2Bi^{3+}Bi^{5+}_{1-2x}Sb^{5+}_{2x}O_6$ samples (50%). The sample preparation technique (citrate pyrolysis) and mixed valence states of Tb are expected to be reflected in this performance. The outcomes show the importance of charge separation mechanisms in the preparation of a novel photocatalyst. In contrast, the improvement in photocatalytic performance is found to be completely related to the Sb substitution dependent reduced particle size and modified surface morphology (from SEM image analysis) for the rare-earth-free samples. However, the performance is comparatively better if it can be considered from the perspective of Sb-free, rare-earth-based compounds. This finding shows the possibility of designing a unique photocatalyst under Sb incorporation.

Furthermore, phase stability and band edge position calculation were strongly supported to this result. As a consequence, phase stability is found to be higher towards unity as the Sb contribution increases in the double perovskite compounds. On the other hand, the calculation of the band edge potential makes it evident that the samples significantly attained higher reduction potential with larger Sb values. As a result, oxidative to reductive photocatalyst as a function of smaller and larger Sb values was observed in the rare-earth-based $Ba_2Tb(Bi_{1-x}Sb_x)O_6$ compounds. Furthermore, band edge potential calculations suggested that heavily Sb-substituted compounds facilitated photocatalytic redox reactions and created more active sites on the sample surface, which resulted in enhanced MB degradation performance. On the other hand, the smaller band gap associated with lower Sb content samples' band edge potential promoted more holes in the VB and highly contributed to the photocatalytic IPA oxidation reaction. These results show a good relationship between photocatalytic efficiency and Sb substitution. Moreover, Machine learning program employed to this research in case of $Ba_2Tb(Bi_{1-x}Sb_x)O_6$ to predict suitable composition is perfectly matched with the experimental result.

Chapter 5

Future Work

To further this line of inquiry, the following researches are proposed:

I. As discussed, the ability of machine learning program to predict suitable material. Therefore, by utilizing this advantage, a novel photocatalytic material can be developed based on the appropriate cation selection with a minimum experiment in the future.

II. It has been observed that the efficiency of a photocatalyst somehow shows much better in the film sample than in powder form. Taking this into account, by preparing $Ba_2(Pr,Tb)(Bi,Sb)O_6$ film samples using electrophoretic deposition approach, further catalytic activities can be discovered in the future.

III. It is known that the energy band engineering of two different catalysts reflected enhanced catalytic performance for Z-scheme photocatalysts. Accordingly, by making Z-schemes with lower Sb-substituted ones (oxidative) and higher Sb-substituted ones (reductive), their photocatalytic properties can be further investigated.

ACKNOWLEDGEMENTS

First and foremost, I would like to express my sincere gratitude and adoration to God, the supreme being, who has bestowed upon the author innumerable favors, understanding, and prospects, enabling me to complete the thesis at last.

Specially, I would like to share my heartfelt gratitude to my supervisor, Professor Dr. Michiaki Matsukawa sensei, for his unwavering guidance and support over the years. His unwavering guidance persisted in the face of my inquiries regarding emerging research subjects, ongoing studies, and even personal matters. Moreover, he provided me with a plethora of invaluable opportunities that significantly advanced my academic trajectory.

In addition, I would like to extend my gratitude to the committee members, Prof. Kazume Nishidate sensei and Prof. Nakanishi Yoshiki sensei, and collaborators Prof. Sumio Aisawa, Prof. Akiyuki Matsushita, Prof. Lin Shiqi, and Hajime Yamamoto sensei for their enduring support in the publication of my research articles and for granting me the chance to present my doctoral research.

I appreciate the assistance of my research team members (Minami Arakida, Hanako Sakou, Kazuto Hata, and others) throughout the collection of experimental data. Specially, the helps from Arakida san and her continuous support during the journey of Doctoral research.

Lastly, I wish to express my gratitude to those who assisted me in improving my quality of life in Japan.

References

[1] A. Fujishima, K. Honda, Electrochemical photolysis of water at a semiconductor electrode, Nature **238**, 37–38 (1972).

[2] M. D. Hern´andez-Alonso, F. Fresno, S. Su´arez, J. M. Coronado, Development of alternative photocatalysts to TiO_2: challenges and opportunities, Energy & Environ. Sci. **2,** 1231–1257 (2009).

[3] A. Nikokavoura, C. Trapalis, Alternative photocatalysts to TiO_2 for the photocatalytic reduction of CO_2, Appl. Surf. Sci. **391,** 149–174 (2017).

[4] N. Daneshvar, D. Salari, A. Khataee, Photocatalytic degradation of azo dye acid red 14 in water on ZnO as an alternative catalyst to TiO_2, *J. Photochem. Photobiol., A* **162,** 317–322 (2004).

[5] F. Temerov, Y. Baghdadi, E. Rattner, S. Eslava, A Review on Halide Perovskite-Based Photocatalysts: Key Factors and Challenges, *ACS Appl. Energy Mater.* **5**, 14605–14637 (2022).

[6] N. M. Gupta, Factors affecting the efficiency of a water splitting photocatalyst: a perspective, *Renew. Sust. Energ. Rev.* **71**, 585–601 (2017).

[7] L. Lu, S. Ni, G. Liu, X. Xu, Structural dependence of photocatalytic hydrogen production over La/Cr co-doped perovskite compound $ATiO_3$ (A= Ca, Sr and Ba), *Int. J. Hydrog. Energy* **42,** 23539–23547 (2017).

[8] K. Maeda, K. Domen, Surface nanostructures in photocatalysts for visible-light-driven water splitting, *Photocatalysis* **303**, 95–119 (2011).

[9] M. Batzill, Fundamental aspects of surface engineering of transition metal oxide photocatalysts, *Energy & Environ. Sci.***4**, 3275–3286 (2011).

[10] M. A. Henderson, A surface science perspective on TiO_2 photocatalysis, *Surf. Sci. Rep.* **66,** 185–297 (2011).

[11] X. Chen, S. Shen, L. Guo, S. Mao, Semiconductor-based photocatalytic hydrogen generation, *Chem. Rev.* **110**, 6503–6570 (2010).

[12] D. Sudha, P. Sivakumar, Review on the photocatalytic activity of various composite catalysts, *Chem. Eng. Process.* **97,** 112–133 (2015).

[13] T. Suzuki, H. Watanabe, Y. Oaki, H. Imai, Tuning of photocatalytic reduction by conduction band engineering of semiconductor quantum dots with experimental evaluation of the band edge potential, *Chem. Commun.* **52,** (2016) 6185–6188.

[14] J. Shi, L. Guo, ABO_3-based photocatalysts for water splitting, Prog. *Nat. Sci.* **22**, 592–615 (2012).

[15] P. Kanhere, Z. Chen, A review on visible light active perovskite-based photocatalysts, *Molecules* **19**, 19995–20022 (2014).

[16] E. Grabowska, Selected perovskite oxides: Characterization, preparation and photocatalytic properties—A review, *Appl. Catal. B* **186**, 97–126 (2016).

[17] J.W. Tang, Z.G. Zou, J.H. Ye, Efficient photocatalysis on $BaBiO_3$ driven by visible light, *J. Phys. Chem. C* **111**, 12779–12785 (2007).

[18] B. Men, J. Zhang, C. Diao, X. Liu, H. Zheng, Photoluminescence, surface photovoltage and photocatalytic properties of $BaBiO_3$ powders, *J. Mater. Sci. Mater. Electron.* **29**, 12729—12734 (2018).

[19] S. Vasala, M. Karppinen, $A_2B'B''O_6$ perovskites: a review, *Prog. Solid State Chem.* **43**, 1–31 (2015).

[20] T. Hatakeyama, S. Takeda, F. Ishikawa, A. Ohmura, A. Nakayama, Y. Yamada, A. Matsushita, Photocatalytic activities of Ba_2RBiO_6 (R= La, Ce, Nd, Sm, Eu, Gd, Dy) under visible light irradiation, J. Yea, *J. Ceram. Soc. Jpn* **118**, 91–95 (2010).

[21] A. Matsushita, T. Nakane, T. Naka, H. Isago, Y. Yamada, Valence States of Rare-Earth Ions and Band Gaps in $RBiBa_2O_6$ (R= La, Ce, Pr, Nd, Sm, Gd, Eu, and Dy) Photocatalysts, *J. Appl. Phys.* **51**, 121802-1-5 (2012).

[22] A. Sato, M. Matsukawa, H. Taniguchi, S. Tsuji, K. Nishidate, S. Aisawa, A. Matsushita, K. Zhang, Structural, physical and photocatalytic properties of mixed-valence double-perovskite $Ba_2Pr(Bi, Sb)O_6$ semiconductor synthesized by citrate pyrolysis technique, *Solid State Sci.* **107**, 106352 (2020).

[23] W.T.A. Harrison, K.P. Reis, A.J. Jacobson, L.F. Schneemeyer, J.V. Waszczak, Syntheses, structures, and magnetism of barium/rare-earth/bismuth double perovskites. Crystal structures of Ba_2MBiO_6 (M= Ce, Pr, Nd, Tb, Yb) by powder neutron diffraction, *Chem. Mater.* **7**, 2161–2167 (1995).

[24] H. Taniguchi, M. Matsukawa, K. Onodera, K. Nishidate, A. Matsushita, Magnetic States and Bandgaps of B-Site Substituted Double-Perovskite $Ba_2Pr(Bi, Sb)O_6$, *IEEE Trans. Magn.* **55**, 2400404-1-4 (2019).

[25] T. Senzaki, M. Matsukawa,T. Yonai, H. Taniguchi, A. Matsushita,T. Sasaki, M. Hagiwara, Chap. 9 In: Functional Materials Synthesis and Physical Properties, ed by M. Bartoli (IntechOpen, 2022). https://doi.org/10.5772/intechopen. 100241.

[26] A.M. Huerta-Flores, D. Sánchez-Martínez, M. del Rocío Hernández-Romero, M.E. Zarazua-Morin, L.M. Torres-Martínez, Visible-light-driven BaBiO3 perovskite photocatalysts: Effect of physicochemical properties on the photoactivity towards water splitting and the removal of rhodamine B from aqueous systems, *J. Photochem. Photobiol. A Chem.* **368**, 70–77 (2019).

[27] F. Izumi, K. Momma, Three-dimensional visualization in powder diffraction, *Solid State Phenom.* **130**, 15–20 (2007).

[28] M. Kawachi, N. Sato, E. Suzuki, S. Ogawa, K. Noto, M. Yoshizawa, Fabrication of $YBa_2Cu_4O_8$ films by electrophoretic deposition technique, *Physica C* **357–360**, 1023–1026 (2001).

[29] P. Giannozzi, S. Baroni, N. Bonini, M. Calandra, R. Car, C. Cavazzoni, D. Ceresoli, G. L. Chiarotti, M. Cococcioni, I. Dabo, et al., Quantum espresso: a modular and open-source software project for quantum simulations of materials, *J. Phys. Condens. Matter* **21**, 395502 (2009).

[30] P. Giannozzi, O. Andreussi, T. Brumme, O. Bunau, M. B. Nardelli, M. Calandra, R. Car, C. Cavazzoni, D. Ceresoli, M. Cococcioni, Advanced capabilities for materials modelling with Quantum ESPRESSO, *J. Phys. Condens. Matter* **29**, 465901 (2017).

[31] J.P. Perdew, K. Burke, M. Ernzerhof, Generalized gradient approximation made simple, *Phys. Rev. Lett.* **77**, 3865–3868 (1996).

[32] A. Dal Corso, Pseudopotentials periodic table: From H to Pu, *Comput. Mater. Sci.* **95**, 337–350 (2014).

[33] P. Giannozzi, S. Baroni, N. Bonini, M. Calandra, R. Car, C. Cavazzoni, D. Ceresoli, G. L. Chiarotti, M. Cococcioni, I. Dabo, A. D. Corso, S. de Gironcoli, S. Fabris, G. Fratesi, R. Gebauer, U. Gerstmann, C. Gougoussis, A. Kokalj, M. Lazzeri, L. Martin-Samos, N. Marzari, F. Mauri, R. Mazzarello, S. Paolini, A. Pasquarello, L. Paulatto, C. Sbraccia, S. Scandolo, G. Sclauzero, A. P. Seitsonen, A. Smogunov, P. Umari, R. M. Wentzcovitch, Quantum espresso: a modular and open-source soft-ware project for quantum simulations of materials, *J. Phys. Condensed Matter* **21**, (39) 395502 (2009).

[34] P. Giannozzi, O. Andreussi, T. Brumme, O. Bunau, M. B. Nardelli, M. Calandra, R. Car, C. Cavazzoni, D. Ceresoli, M. Cococcioni, et al., Advanced capabilities for materials modelling with quantum espresso, *J. Phys. Condensed Matter* **29,** (46) 465901 (2017).

[35] J. Heyd, G.E. Scuseria, M. Ernzerhof, Hybrid functionals based on a screened Coulomb potential, *J. Chem. Phys.* **118,** (18) 8207–8215 (2003).

[36] J. Heyd, G.E. Scuseria, M. Ernzerhof, Erratum: "Hybrid functionals based on a screened Coulomb potential, *J. Chem. Phys.* **124**, (21) 219906 (2006).

[37] A.A. Mostofi, J.R. Yates, Y.-S. Lee, I. Souza, D. Vanderbilt, N. Marzari, wannier90: A tool for obtaining maximally-localised Wannier functions, Comput. Phys. Commun. **178**, (9) 685–699 (2008).

[38] N. Marzari, D. Vanderbilt, Maximally localized generalized Wannier functions for composite energy bands, Phys. Rev. B **56,** (20) 12847 (1997).

[39] I. Souza, N. Marzari, D. Vanderbilt, Maximally localized Wannier functions for entangled energy bands, *Phys. Rev. B* **65,** (3) 035109 (2001).

[40] N. Marzari, A.A. Mostofi, J.R. Yates, I. Souza, D. Vanderbilt, Maximally localized Wannier functions: Theory and applications, *Rev. Modern Phys.* **84,** (4) 1419 (2012).

[41] W. Wang, N. Xie, L. He, Y. Yin, Photocatalytic colour switching of redox dyes for ink-free light-printable rewritable paper, *Nat. Commun.* **5**, 5459 (2014).

[42] Y.N. Liu, X. Zhou, X. Wang, K. Liang, X.K. Yang, C.C. Shen, M. Imran, S. Sahar, A.W. Xu, An efficient strategy for full mineralization of an azo dye in wastewater: A synergistic combination of solar thermo-and electrochemistry plus photocatalysis, *RSC Adv.* **7**, 36246—36255 (2017).

[43] T. Murase, H. Irie, K. Hashimoto, Visible light sensitive photocatalysts, nitrogen-doped Ta_2O_5 powders, *J. Phys. Chem. B* **108**, 15803–15807 (2004).

[44] R. Mangalam, E. Suard, A. Sundaresan, Crystal structure and dielectric properties of ordered perovskites Ba_2BiSbO_6 and $BaSrBiSbO_6$, *Physica B* **404,** (1) 154–157 (2009).

[45] W. Fu, A neutron powder diffraction study on $BaBi_{0.5}Sb_{0.5}O_3$, *Solid State Commun.* **116,** (8) 461–464 (2000).

[46] W. Fu, R. de Gelder, R. de Graaff, Crystal structure of the ordered per-ovskite: $BaBi_{0.5}Sb_{0.5}O_3$, *Materials Research Bulletin* **32,** (6) 657–662 (1997).

[47] X. Li, Y. Luo, X. Liu, Preparation and electrical properties of perovskite ceramics in the system $BaBi_{1-x}Sb_xO_3$ ($0 \leq x \leq 0.5$), *J. Alloys Compd.* **509,**(17) 5373–5375 (2011).

[48] M. Yasukawa, Y. Shiga, T. Kono, Electrical conduction and thermoelectric properties of perovskite-type $BaBi_{1-x}Sb_xO_3$, *Solid State Commun.* **152**, (11) 964–967 (2012).

[49] C. Chaillout, J. Remeika, A. Santoro, M. Marezio, The determination of the Bi valence state in BaBiO3 by neutron powder diffraction data, *Solid State Commun.* **56,** (10) 829–831 (1985).

[50] A.W. Sleight, Bismuthates: BaBiO3 and related superconducting phases, *Phys. C: Supercond. Appl*. **514**, 152–165 (2015).

[51] S. Otsuka, Y. Hinatsu, Structures and magnetic properties of rare earth double perovskites containing antimony or bismuth Ba_2LnMO_6 (Ln= rare earths; M= Sb, Bi), *J. Solid State Chem.* **227**, 132–141 (2015).

[52] We estimated the ratio (y) by using $\mu_{eff}^2 = y\mu_{eff}^2(Tb^{3+}) + (1-y)\mu_{eff}^2(Tb^{4+})$ with $\mu_{eff}(Tb^{3+}) = 9.72\ \mu_B$, $\mu_{eff}(Tb^{3+}) = 7.94\ \mu_B$.

[53] K. Onodera, T. Kogawa, M. Matsukawa, H. Taniguchi, K. Nishidate, A. Matsushita, M. Shimoda, Magnetic, thermodynamic and optical properties of Sb-substituted Ba_2PrBiO_6 double perovskite oxides, *J. Phys. Conf. Ser.* **969**, 012122-1-6 (2018).

[54] R. Shannon, Revised effective ionic radii and systematic studies of interatomic distances in halides and chalcogenides, *Acta Crystallogr. A* **32**, 751 (1976).

[55] W.T. Fu, D.J.W. Ijdo, X-ray and neutron powder diffraction study of the double perovskites Ba_2LnSbO_6 (Ln= La, Pr, Nd and Sm, *J. Solid State Chem.* **178**, 2363–2367 (2005).

[56] P.J. Saines, B.J. Kennedy, M.M. Elcombe, H.H. Harris, L.Y. Jang, Z. Zhang, Phase and valence transitions in $Ba_2LnSn_xSb_{1-x}O_{6-\delta}$ (Ln= Pr and Tb), *J. Solid State Chem.* **181**, 2941–2952 (2008).

[57] S. Otsuka, Y. Hinatsu, Structures and magnetic properties of rare earth double perovskites containing antimony or bismuth Ba_2LnMO_6 (Ln= rare earths; M= Sb, Bi), *J. Solid State Chem.* **227,** 132–141 (2015).

[58] A. Mazzoli, O. Favoni, Particle size, size distribution and morphological evaluation of airborne dust particles of diverse woods by scanning electron microscopy and image processing program, Powder Technology **225**, 65–71 (2012).

[59] K. Nishidate, A. Adiko, M. Matsukawa, H. Taniguchi, A. Sato, A. Matsushita, S. Tanibayashi, M. Hasegawa, Electronic properties and crystal structures of double-perovskites, $Ba_2Bi^{III}Bi^{V}O_6$, Ba_2PrBiO_6, and Ba_2PrSbO_6: First-principles study, *Mater. Res. Express* **7**, 065505-1-8 (2020).

[60] C. Franchini, A. Sanna, M. Marsman, G. Kresse, Structural, vibrational, and quasiparticle properties of the Peierls semiconductor $BaBiO_3$: A hybrid functional and self-consistent GW+ vertex-corrections study, *Phys. Rev. B* **81**, 085213-1-7 (2010).

[61] D. Roy, M. Matsukawa, T. Yonai, M. Arakida, H. Taniguchi, K. Nishidate, S. Aisawa, A. Matsushita, L. Shiqi, Enhanced photocatalytic activities under visible light of double-perovskite oxide semiconductor Ba2Tb (Bi, Sb) O6 with mixed-valence *J. Mater. Sci., Mater. Electron.* **34,** (4) 281 (2023).

[62] B.J. Kennedy, C.J. Howard, K.S. Knight, Z. Zhang, Q. Zhou, Structures and phase transitions in the ordered double perovskites $Ba_2Bi^{III}Bi^{V}O_1$ and $Ba_2Bi^{III}Sb^{V}O_6$, *Acta Crystallogr. B* **62**, (4) 537–546 (2006).

[63] C. Franchini, A. Sanna, M. Marsman, G. Kresse, Structural, vibrational, and quasiparticle properties of the Peierls semiconductor $BaBiO_3$: A hybrid functional and self-consistent GW+ vertex-corrections study, *Phys. Rev. B* **81**, (8) 085213 (2010).

[64] R. Tamura, T. Osadab, K. Minagawa, T. Kohata, M. Hirosawa, K. Tsuda, K. Kawagishi, Machine learning-driven optimization in powder manufacturing of Ni-Co based superalloy, *Mater. Des.* **198**, 109290-1-11 (2021).

[65] K. Terayama, K. Tsuda, R. Tamura, Efficient recommendation tool of materials by an executable file based on machine learning, *Jpn. J. Appl. Phys.* **58**, 098001-1-4 (2019).

[66] A. Dodd, A. McKinley, M. Saunders, T. Tsuzuki, Effect of particle size on the photocatalytic activity of nanoparticulate zinc oxide, *J. Nanopart. Res.* **8**, 43–51 (2006).

[67] T. Edvinsson, Optical quantum confinement and photocatalytic properties in two-, one-and zerodimensional nanostructures, *R. Soc. Open Sci.* **5**, (9) 180387 (2018).

[68] P. Amalthi, J. Judith Vijaya, L. John Kennedy, A. Mustafa, M. Bououdina, Magnetically recoverable $Nd_{0.7}Ca_{0.3}Mn_{1-x}Ni_xO_3$ polygonal-shaped perovskite nanophotocatalysts for efficient visible-light degradation of methylene blue and tetracycline, *J. Phys. Chem. Solids* **169**, 110860-1-17 (2022).

[69] H. Yang, C. Han, X. Xue, Photocatalytic activity of Fe-doped $CaTiO_3$ under uv–visible light, *J. Environ. Sci.* **26**, 1489–1495 (2014).

[70] N.S. Abdul Satar, R. Adnan, H.L. Lee, S.R. Hall, T. Kobayashi, M.H. Mohamad Kassim, K.N.H. Mohd, Facile green synthesis of ytrium-doped $BiFeO_3$ with highly

efficient photocatalytic degradation towards methylene blue, *Ceram. Int.* **45**, 15964–15973 (2019).

[71] L. Wang, H. Gu, J. He, T. Zhao, X. Zhang, C. Xiao, H. Liu, X. Zhang, Y. Li, Scale synthesized cubic $NaNbO_3$ nanoparticles with recoverable adsorption and photodegradation for prompt removal of methylene blue, *J. Alloys Compd.* **695**, 599–606 (2017).

[72] M.A. Butter, D.S. Ginley, Prediction of flatband potentials at semiconductor-electrolyte interfaces from atomic electronegativities, *J. Electrochem. Soc.* **125**, 228–232 (1978).

[73] A.H. Nethercot, Prediction of Fermi energies and photoelectric thresholds based on electronegativity concepts, *Phys. Rev. Lett.* **33**, 1088–1091 (1974).